

Human single cell RNA-sequencing reveals a targetable CD8⁺ exhausted T cell population that maintains mouse low-grade glioma growth

Received: 7 November 2023

Accepted: 14 November 2024

Published online: 28 November 2024



Rasha Barakat¹, Jit Chatterjee¹, Rui Mu¹, Xuanhe Qi¹, Xingxing Gu², Igor Smirnov², Olivia Cobb¹, Karen Gao¹, Angelica Barnes¹, Jonathan Kipnis² & David H. Gutmann¹✉

In solid cancers, T cells typically function as cytotoxic effectors to limit tumor growth, prompting therapies that capitalize upon this antineoplastic property (immune checkpoint inhibition; ICI). Unfortunately, ICI treatments have been largely ineffective for high-grade brain tumors (gliomas; HGGs). Leveraging several single-cell RNA sequencing datasets, we report greater CD8⁺ exhausted T cells in human pediatric low-grade gliomas (LGGs) relative to adult and pediatric HGGs. Using several preclinical mouse LGG models (*Nf1*-OPG mice), we show that these PD1⁺/TIGIT⁺ CD8⁺ exhausted T cells are restricted to the tumor tissue, where they express paracrine factors necessary for OPG growth. Importantly, ICI treatments with α -PD1 and α -TIGIT antibodies attenuate *Nf1*-OPG tumor proliferation through suppression of two cytokine (Ccl4 and TGF β)-mediated mechanisms, rather than by T cell-mediated cytotoxicity, as well as suppress monocyte-controlled T cell chemotaxis. Collectively, these findings establish a previously unrecognized function for CD8⁺ exhausted T cells as specialized regulators of LGG maintenance.

Gliomas, the most common brain tumors in children and adults, are classified by the World Health Organization (WHO) as low- (grades 1 and 2) or high- (grades 3 and 4) grade tumors. HGG, like glioblastoma, predominate in the adult population and differ from LGGs by their rapid growth, microvascular proliferation, necrosis, and poor prognosis¹. In contrast, LGGs, including pilocytic astrocytoma (PA; grade 1), account for the majority of pediatric brain tumors and are associated with good overall survival rates². The neoplastic cells in these gliomas are embedded within a microenvironment rich in immune cells, including tumor-associated monocytes (macrophages, microglia) and lymphoid cells³. Within this stromal cell compartment, T cells (conventional CD4⁺ T cells, regulatory CD4⁺ T cells, and CD8⁺ cytotoxic T lymphocytes) constitute 0–5% of the total tumor cellular

content^{4,5}. Typically, the CD8⁺ T cells in these tumors are thought to function as “effector” (cytotoxic) T cells, which can recognize antigens expressed or shed by the neoplastic cells (“tumor neoantigens”). When activated, these effector T cells limit glioma growth by killing the tumor cells^{6,7}. Considerable efforts have focused on harnessing their anti-tumoral capabilities for therapeutic purposes by reactivating them from an exhausted (non-reactive) state. Exhausted T cells are characterized by increased expression of cytotoxic T-lymphocyte-associated protein 4 (CTLA4), T cell immunoglobulin and mucin-domain containing-3 (TIM3), ectonucleoside triphosphate diphosphohydrolase 1 (CD39), T cell immunoreceptor with Ig and ITIM domains (TIGIT), lymphocyte activating 3 (LAG3), and programmed cell death protein-1 (PD1). The latter antigen serves as the target for

¹Department of Neurology, Washington University School of Medicine, St. Louis, MO 63110, USA. ²Department of Pathology and Immunology, Washington University School of Medicine, St. Louis, MO 63110, USA. ✉e-mail: gutmann@wustl.edu

many immune checkpoint therapies that release exhausted T cells from their non-reactive state and allows them to kill malignant cancer tumor cells^{8,9}.

Unfortunately, ICI therapy has not proven efficacious for malignant brain tumors, like glioblastoma¹⁰. This outcome could reflect a relative paucity of canonical CD8⁺ exhausted T cells in these “ICI therapy non-responsive” tumors¹¹. For this reason, we leveraged single cell RNA sequencing data from three independent sets of pilocytic astrocytoma (PA)^{12,13}, as well as several adult and pediatric HGG datasets^{14–16}, to reveal an enrichment of PD1⁺ and TIGIT⁺ CD8⁺ exhausted T cells in PAs relative to their malignant pediatric and adult HGG counterparts.

To explore the contribution of CD8⁺ T cells to LGG growth in an immunologically intact mouse system in vivo, we used the only currently available authenticated preclinical mouse models of pediatric LGG – those that recapitulate the genetics of the neurofibromatosis type 1 (NF1) cancer predisposition syndrome, in which children develop LGGs of the optic nerve and chiasm^{17,18}. Similarly, *Nf1*-mutant mice develop optic nerve and chiasm LGGs (optic pathway gliomas; OPG) in a highly penetrant and reproducible manner by 12 weeks of age¹⁹. In these *Nf1*-OPG mice, CD8⁺ T cells²⁰ are stimulated by midkine produced by *Nf1*-mutant neurons²¹. This results in the elaboration of Ccl4 by CD8⁺ T cells to induce tumor-associated monocyte (TAM) expression of Ccl5, a mitogen required for *Nf1*-OPG growth²².

Herein, we demonstrate that Ccl4-producing PD1⁺ and TIGIT⁺ CD8⁺ exhausted T cells are restricted to the tumors of *Nf1*-OPG mice. In these tumors, CD8⁺ exhausted T cell-mediated tumor growth is mediated by both Ccl4 TAM activation and a second TGFβ-dependent effect on tumor cell proliferation. In this regard, α-PD1 ICI treatment reduces TGFβ-mediated tumor cell growth, while combined α-PD1/α-TIGIT ICI therapy abrogates Ccl4-controlled TAM production of Ccl5. Similar to Ccl5 or TAM targeting, neutralizing α-TGFβ antibodies reduce *Nf1*-OPG growth in vivo. Additionally, we elucidate a second T cell chemoattraction circuit involving TAM production of Ccl12 and Cxcl13, which is abrogated by ICI treatment. Taken together, these findings establish unexpected roles for this specialized population of T lymphocytes in brain tumor biology relevant to immune targeted therapies.

Results

CD8⁺ exhausted T cells are enriched in human and mouse low-grade glioma relative to high-grade gliomas

Clinical trials using ICI therapy have shown efficacy for some malignant tumors, including melanomas, non-small-cell lung carcinomas (NSCLC), and breast cancer^{23,24}. In contrast, this immune-targeted approach has not been successful for the treatment of glioblastoma⁹. Leveraging published single cell RNA-sequencing (scRNAseq) datasets from human pediatric LGG^{12,13} (pLGG, PA) (grade 1 glioma; pilocytic astrocytoma [PA], GSE222850 and dbGAP phs001854.v1.p1), pediatric HGG¹⁶ (pHGG) (grade 4 diffuse midline glioma [DMG], GSE102130), and adult HGG (aHGG) (grade 4 glioblastoma^{14,15} [GBM], Annotare [ArrayExpress] accession # E-MTAB-9435 and GSE138794), we found that PAs harbor greater T cell content (11.88% T cells, pediatric LGG; 0.18% T cells, adult HGG; 0.09% T cells, pediatric HGG) (Fig. 1A, B), increased *CD8A* gene expression (Fig. 1C, D), and higher expression of classic exhaustion markers²⁵ (*TIGIT*, *PDCDI*, *LAG3*, and *CTLA4*; Fig. 1E), than HGGs. To study CD8⁺ exhausted T cells in human PAs, we performed scRNAseq of four sporadic and one NF1-associated tumors from the Pediatric Brain Tumor Repository at St. Louis Children's Hospital. Unsupervised clustering identified multiple cell types, including endothelial cells, TAM, neurons, T cells, and tumor cells (Fig. 1F, G, Supplementary Fig. 1A, D). Within the CD8⁺ T cell cluster, a subset of expressed genes and pathways associated with T cell exhaustion (*PDCDI*, *TIGIT*, and *LAG3*; Fig. 1H–J, Supplementary Fig. 1B, C, E, F, O), regardless of NF1 disease status (Supplementary Fig. 1A–F).

Moreover, these T cells also expressed cytokines and effector molecules typically associated with a canonical exhausted T cell phenotype²⁶. This CD8⁺ exhausted T cell population was also found in two additional independently generated human PA datasets from Boston Children's Hospital and KITZ (Heidelberg University; Supplementary Fig. 1G–N).

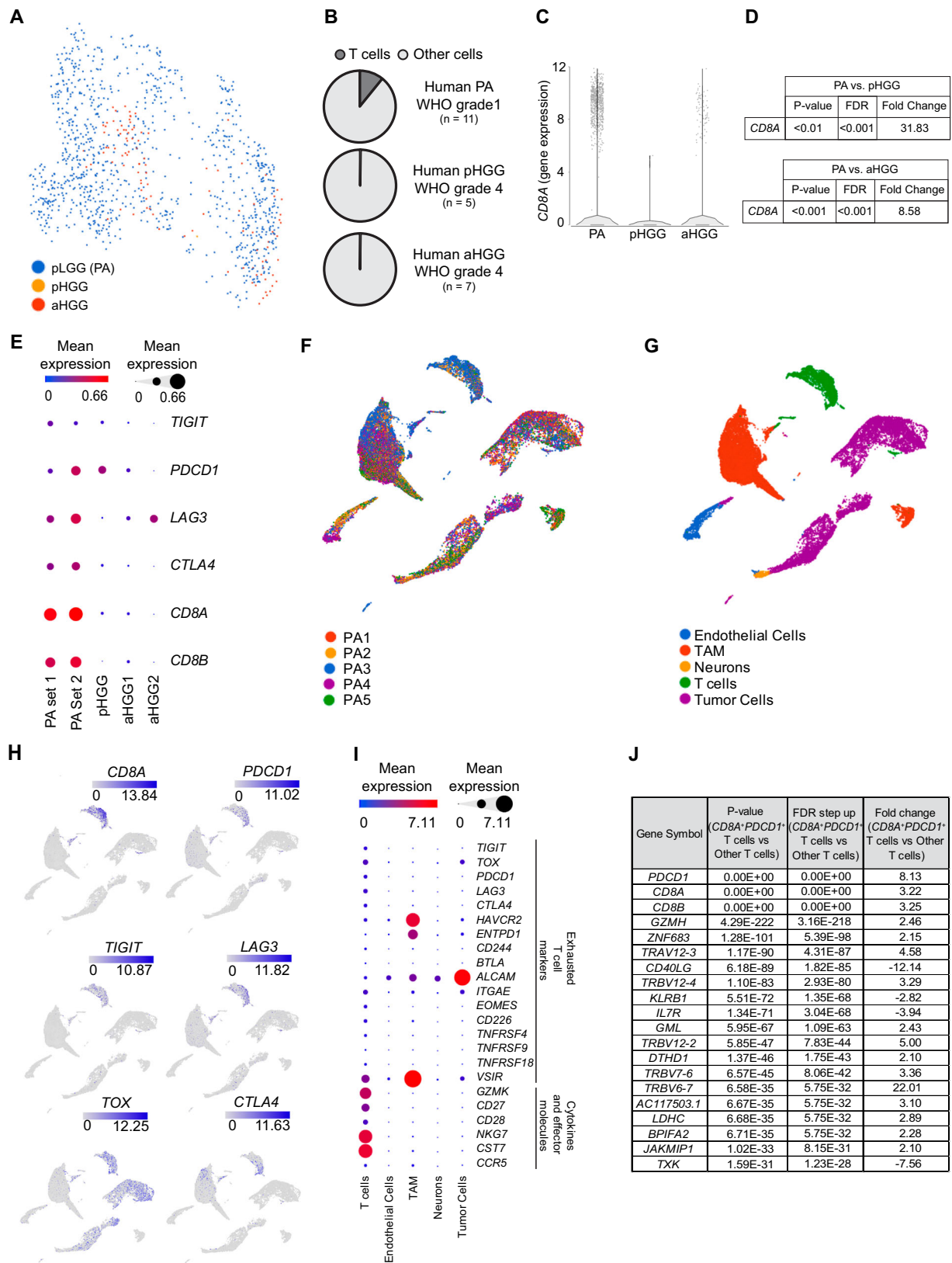
To confirm the existence of CD8⁺ exhausted T cells in mouse LGGs, scRNAseq was performed on optic nerves from two independent cohorts of *Nf1*-OPG mice (Fig. 2A, Supplementary Fig. 2A). Similar to their human counterparts, we identified a CD8⁺ exhausted T cell population expressing *Pdcd1*, *Tigit*, *Tox*, and *LAG3* in both cohorts, as well as cytokines, effector molecules, and pathways associated with exhaustion (Fig. 2B, C, Supplementary Fig. 2B, C, E, F). T cell receptor (TCR) sequencing revealed that the highest frequency clonotype corresponded to this CD8⁺ exhausted population (Fig. 2D, Supplementary Fig. 2D). Further analysis of the exhausted T cell populations in the mouse datasets revealed that the CD8⁺ exhausted T cell cluster comprised T cells expressing terminal exhaustion markers (terminally exhausted T cells, TEX; *Pdcd1*⁺ *Havcr2*⁺ *Tcf7*⁺), *CD39*/*Entpd1*²⁷, and progenitor exhaustion markers (progenitor exhausted T cells, PEX, *Pdcd1*⁺ *Havcr2*⁺ *Tcf7*⁺) (Supplementary Fig. 2G)²⁸. Taken together, these findings identify a unique population of CD8⁺ exhausted T cells in both human and mouse LGGs.

CD8⁺ exhausted T cells are enriched in the optic nerves of tumor-bearing mice

Next, we sought to define the tissue compartments in which CD8⁺ exhausted T cells reside in *Nf1*-OPG mice (Fig. 3A). While CD8⁺ exhausted T cells were not detected in peripheral blood mononuclear cells (PBMCs) from *Nf1*-OPG mice by scRNAseq (Fig. 3B, C), a CD8⁺ exhausted-like population with low level (*Tigit*, *Tox*, *Pdcd1*) or no (*LAG3*, *Cst7*, *Ctla4*, *Tnfrsf9*, *Cd27*, *Cd28*) expression of exhaustion markers was detected in the dura (Fig. 3D, E). Following gating on live single cells, the PD1⁺ TIGIT⁺ CD8⁺ exhausted population was not found in WT or *Nf1*^{+/−} mice (Supplementary Fig. 3A–E) or in the PBMCs and deep cervical lymph nodes of 12-week-old *Nf1*-OPG mice (Fig. 3F, I, L). Although a CD8⁺/PD1⁺ population was detected in both the dura and optic nerves of 12-week-old *Nf1*-OPG mice (29.65% CD8⁺/PD1⁺ T cells in the optic nerve; 16.1% CD8⁺/PD1⁺ T cells in the dura), a PD1/TIGIT double-positive CD8⁺ exhausted T cell population was mainly found in the optic nerve (7.87% CD8⁺/PD1⁺/TIGIT⁺ T cells in the optic nerve; 2.75% CD8⁺/PD1⁺/TIGIT⁺ T cells in the dura, 0.17% CD8⁺/PD1⁺/TIGIT⁺ T cells in the PBMCs, 0.03% CD8⁺/PD1⁺/TIGIT⁺ T cells in the dCLN) (Fig. 3G–H, 3J–L, Supplementary Fig. 3G–I). Importantly, CD8⁺ exhausted T cell populations expressing TEX and PEX markers were only found in the optic nerves of tumor-bearing mice, and not in the meningeal dura or PBMC scRNAseq datasets. *CD39* expression was also restricted to the optic nerve TEX population and *Entpd1* (*CD39*) was not present in either the meningeal dura or PBMCs (Supplementary Fig. 3F, 3I). Similar to mouse LGG, a PD1⁺/TIGIT⁺ CD8⁺ exhausted T cell population was also detected in human LGG (PA) tumors using flow cytometry (Fig. 3M, Supplementary Fig. 3J–K).

CD8⁺ exhausted T cells express Ccl4

Relevant to the role of T cells in *Nf1*-OPG tumors, we previously demonstrated that CD8⁺ T cells produce Ccl4 to induce TAM expression of Ccl5, a mitogen required for tumor cell growth (Fig. 4A)^{22,29}, such that CD8⁺ T cell antibody-mediated depletion abrogates *Nf1*-OPG growth in vivo²². To establish the importance of this discovered CD8⁺ exhausted T cell population to *Nf1*-OPG growth, we performed a series of complementary experiments: First, by RT-qPCR, we showed that *Ccl4* was highly expressed in the optic nerves (tumor site) of 12-week-old *Nf1*-OPG mice relative to non-tumor-containing brain regions (cerebellum, brainstem, cortex, hippocampus) or tissues where T cells circulate (dura, deep cervical lymph nodes, superficial cervical lymph



nodes) (Fig. 4B). Second, using scRNAseq, we demonstrated that *Ccl4* expression was enriched in CD8⁺ exhausted T cells from the optic nerves relative to other tissues (Fig. 4C), other optic nerve T cell populations (fold change=2.67, $P=2.63E-6$, Fig. 4D; fold change=5.90, $P=3.52E-18$, Supplementary Fig. 4A; fold change=1.81, $P=6.71E-15$, Supplementary Fig. 4B), CD4⁺ Treg cells (fold change=

4.01, $P=2.06E-3$, Supplementary Fig. 4C; fold change=7.31, $P=4.09E-15$, Supplementary Fig. 4D), PBMC T cells (fold change=8.40, $P=5.95E-31$, Fig. 4E), and dural T cells (fold change=2.52, $P=3.8E-31$, Fig. 4F). Additionally, the *Ccl4*-expressing T cells in the optic nerves of *Nf1*-OPG mice show an enrichment in genes and pathways related to cytokine activity and chemokine binding

Fig. 1 | CD8⁺ exhausted T cells are present in human pilocytic astrocytomas. **A** UMAP visualization of T cells from human pLGG ([pilocytic astrocytoma, PA] PA set 1 and PA set 2 datasets; WHO grade 1 PA tumors) ($n = 2$ datasets, 11 tumors, GSE222850 and dbGAP phs001854.v1.p1), human pediatric HGG (pHGG [diffuse midline glioma, DMG] datasets; WHO grade 4 tumors) ($n = 1$ dataset, 5 tumors, GSE102130), and human adult HGG ([glioblastoma, GBM], aHGG1 and aHGG2 datasets; WHO grade 4 tumors) ($n = 2$ datasets, 7 tumors, Annotare [ArrayExpress] accession # E-MTAB-9435 and GSE138794) scRNAseq datasets. **B** Charts showing the percentage of T cells from human PA (PA set 1 and PA set 2 datasets; WHO grade 1 PA tumors) ($n = 2$ datasets, 11 tumors), human pediatric HGG (pHGG [diffuse midline glioma, DMG] datasets; WHO grade 4 tumors) ($n = 1$ dataset, 5 tumors), and human adult HGG ([glioblastoma, GBM], aHGG1 and aHGG2 datasets; WHO grade 4 tumors) ($n = 2$ datasets, 7 tumors) scRNAseq datasets. **C** *CD8A* expression in human PA ($n = 2$ datasets), pediatric HGG ($n = 1$ dataset) and adult HGG samples ($n = 2$ datasets). Each dot is an individual cell. **D** Table showing the *P* value, false discovery

rate (FDR), and fold change of *CD8A* expression in human PA, pediatric and adult HGGs. Differential analyses were performed using gene specific analysis (GSA). **E** Dot plot showing the genes used to identify CD8⁺ exhausted T cells in human PA ($n = 2$) and HGG datasets (pediatric, $n = 1$; adult, $n = 2$). **F** UMAP visualization of scRNAseq data from five human PA specimens (PA1 [4463 cells], PA2 [4829 cells], PA3 [10404 cells], PA4 [7210 cells], PA5 [4636 cells]) based on tumor sample. **G** UMAP visualization of scRNAseq data from five human PA specimens (PA1, PA2, PA3, PA4, PA5) based on cell type. **H** UMAP visualization of scRNAseq data from five human PA specimens (PA1, PA2, PA3, PA4, PA5) color-coded by gene expression (*CD8A*, *PDCDL1*, *TIGIT*, *LAG3*, *TOX*, *CTLA4*). **I** Dot plot showing the genes used to identify CD8⁺ exhausted T cells in human PA specimens. **J** Top 20 transcripts in *CD8A*⁺ *PDCDL1*⁺ T cells relative to other T cells calculated with DESeq2 and filtered *P* values ≤ 0.05 , false discovery rates ≤ 0.1 , and log fold changes greater or equal to ± 2 . Differential analyses were performed using gene specific analysis (GSA).

(Supplementary Fig. 4G, H). While TAM in the optic nerve also express *Ccl4*, monocyte *Ccl4* expression in non-tumor bearing (*Nf1*^{+/−} and WT) is similar to that seen in tumor bearing (*Nf1*-OPG) mice (Supplementary Fig. 4E, F). Moreover, *Ccl4* and *Entpd1* (*CD39*) expression were also enriched in the TEX compared to non-TEX (*Ccl4* fold change = 151.27, $P = 3.25E-9$; *Entpd1* (*CD39*) fold change = 3.86, $P = 5.56E-17$, Fig. 4G) and PEX T cell populations within *Nf1*-OPG mouse optic nerves (*Ccl4* fold change = 26.74, $P = 5.97E-6$; *Entpd1* (*CD39*) fold change = 7.41, $P = 1.99E-11$, Supplementary Fig. 4I).

Third, since we previously showed that CD8⁺ T cell *Ccl4* expression is dependent on NFAT activity²², we stimulated CD8⁺ T cells in vitro with α -CD3/ α -CD28 antibodies to generate CD8⁺ “exhausted” T cells (exhausted). Following exhaustion, CD8⁺ T cells express more *Ccl4* relative to unstimulated CD8⁺ T cells (non-exhausted) (fold change = 8.8, $P < 0.0001$, Fig. 4H). Moreover, following treatment with the FK506 calcineurin inhibitor, *Ccl4* production was reduced (79% decrease, $P < 0.0001$, Fig. 4H), confirming that exhaustion-mediated production of *Ccl4* is NFAT1-dependent. In addition, *Nfatc2* expression was enriched in *Ccl4*-expressing TEX compared to CD8⁺ non-TEX (fold change = 24.13, $P = 1.25E-11$, Fig. 4G) or PEX (fold change = 28.89, $P = 8.73E-8$, Supplementary Fig. 4J) T cells.

Fourth, scRNA-seq analysis revealed that CD8⁺ T cell exhaustion increases during *Nf1*-OPG tumor evolution. No CD8⁺ exhausted T cell cluster was identified at 6 weeks of age at a stage before obvious tumors are found (Fig. 5A, B), but was detected in mice with optic gliomas at both 12 (Fig. 2A–D; Supplementary Fig. 2A–D) and 24 weeks (Fig. 5C, D) of age (Fig. 5E), paralleling changes in tumor proliferation (%Ki67⁺ cells) and *Ccl4*/*Ccl5* expression (Fig. 5F, H–K) during tumor evolution. However, there was no difference in CD8⁺ T cell numbers or the percentage of CD8⁺ exhausted T cells between 12- and 24-week-old tumor-bearing mice (Fig. 5F, G).

Fifth, we analyzed two additional *Nf1*-mutant mouse strains, one that also forms optic gliomas by 12 weeks of age (*Nf1*^{Arg681X})^{30,31} and one that does not develop tumors (*Nf1*^{Arg1809C})²¹. Consistent with a key role for CD8⁺ exhausted T cells in *Nf1*-OPG pathogenesis, PD1⁺/TIGIT⁺ CD8⁺ T cells were only detected by flow cytometry in *Nf1*^{Arg681X}, but not *Nf1*^{Arg1809C}, mice (Supplementary Fig. 5A–C). Taken together, the presence of PD1⁺/TIGIT⁺/CD39⁺ CD8⁺ exhausted T cells exclusively in the optic nerves of tumor-bearing mice, their absence in non-tumor-bearing mice, and their NFAT1-dependent *Ccl4* expression establish CD8⁺ exhausted T cells expressing terminal exhaustion markers as the most likely lymphocyte population within the immune axis that regulates *Nf1*-OPG growth.

Anti-PD1⁺/TIGIT⁺ ICI treatment reduces CD8⁺ T cell infiltration by decreasing TAM-mediated *Ccl12* and *Cxcl13* chemoattraction

To determine whether CD8⁺ exhausted T cells are necessary for *Nf1*-OPG formation, 12-week-old *Nf1*-OPG mice with established tumors were treated with α -PD1 or α -TIGIT antibodies or both (200 μ g/dose,

twice per week) (Fig. 6A). All treatments reduced CD8⁺ T cell content in the tumors (Fig. 6B), and the number of circulating CD8⁺ T cells in the dura (Supplementary Fig. 6A). Previous studies from our group demonstrated that *Ccl2*, produced by *Nf1*-OPG tumor cells, can attract T cells into the tumor^{20,22,32}. However, *Ccl2* was only attenuated following combined α -PD1 and α -TIGIT antibody treatment (75% decrease, $P = 0.0240$) (Fig. 6C), which does not explain the reduction of CD8⁺ T cells in the optic nerves of *Nf1*-OPG mice treated with either α -PD1 or α -TIGIT antibodies.

To elucidate the mechanism responsible for the reduction in CD8⁺ T cell numbers, we first leveraged data from scRNAseq data from 12-week-old *Nf1*-OPG, *Nf1*^{+/−}, and WT mouse optic nerves to identify potential chemokines that might attract T cells into the tumor. Using this approach, there were no additional chemoattractants, besides *Ccl2*, expressed by *Nf1*-OPG tumor cells. However, we identified three potential chemokines expressed by TAM in the optic nerves of *Nf1*-OPG mice relative to *Nf1*^{+/−} and WT optic nerve monocytes (*Ccl12*, *Cxcl9*, and *Cxcl13*) (Fig. 6D). Importantly, the receptors for each of these chemokines/cytokines (*Ccl12*:Ccr2, *Cxcl9*:Cxcr3, *Cxcl13*:Cxcr5) were expressed in CD8⁺ exhausted T cells (Fig. 6E). Second, we performed RT-qPCR analyses using a separate cohort of *Nf1*-OPG and WT optic nerve samples to demonstrate that only *Ccl12* and *Cxcl13*, but not *Cxcl9*, expression was increased in *Nf1*-OPG relative to WT optic nerves (Fig. 6F). Third, using a modified Boyden chamber migration assay, we found that *Ccl12* and *Cxcl13* increased CD8⁺ T cell motility (Fig. 6G). Fourth, to assess *Ccl12* and *Cxcl13* expression in the optic nerves of *Nf1*-OPG mice treated with α -PD1, α -TIGIT and α -PD1 + TIGIT antibody therapies, we performed RT-qPCR and confirmed decreased *Ccl12* (72% decrease, α -TIGIT; 53% decrease, α -PD1; 82% decrease, α -PD1 + TIGIT) and *Cxcl13* (63% decrease, α -TIGIT; 65% decrease, α -PD1; 79% decrease, α -PD1 + TIGIT) expression relative to IgG-treated controls (Fig. 6H–I). Taken together, these results establish that CD8⁺ T cells are attracted by both tumor cells (*Ccl2*) and TAM (*Ccl12* and *Cxcl13*).

Anti-PD1⁺/TIGIT⁺ ICI treatment reduces tumor cell proliferation through two distinct mechanisms

To determine whether *Ccl4*-expressing CD8⁺ exhausted T cells support *Nf1*-OPG growth, we assessed the percentage of proliferating cells in the optic nerves of mice treated with α -PD1 or α -TIGIT antibodies or both. Ki67 was used as a marker of tumor cell proliferation, as the proliferating cells are glioma cells³³, rather than CD3⁺ T cells or Tmem119⁺ TAM as previously shown³² or endothelial cells (Supplementary Fig. 6B, C). While α -TIGIT antibody treatment did not reduce *Nf1*-OPG proliferation, α -PD1 or combined α -PD1 and α -TIGIT antibody treatment decreased tumor proliferation (%Ki67⁺ cells) (Fig. 7A). As observed in other preclinical experiments^{32,34}, optic nerve volumes calculated using Eq.(1) and TAM content (%Iba1⁺ cells) in the optic nerve were not affected by any of the treatments (Supplementary

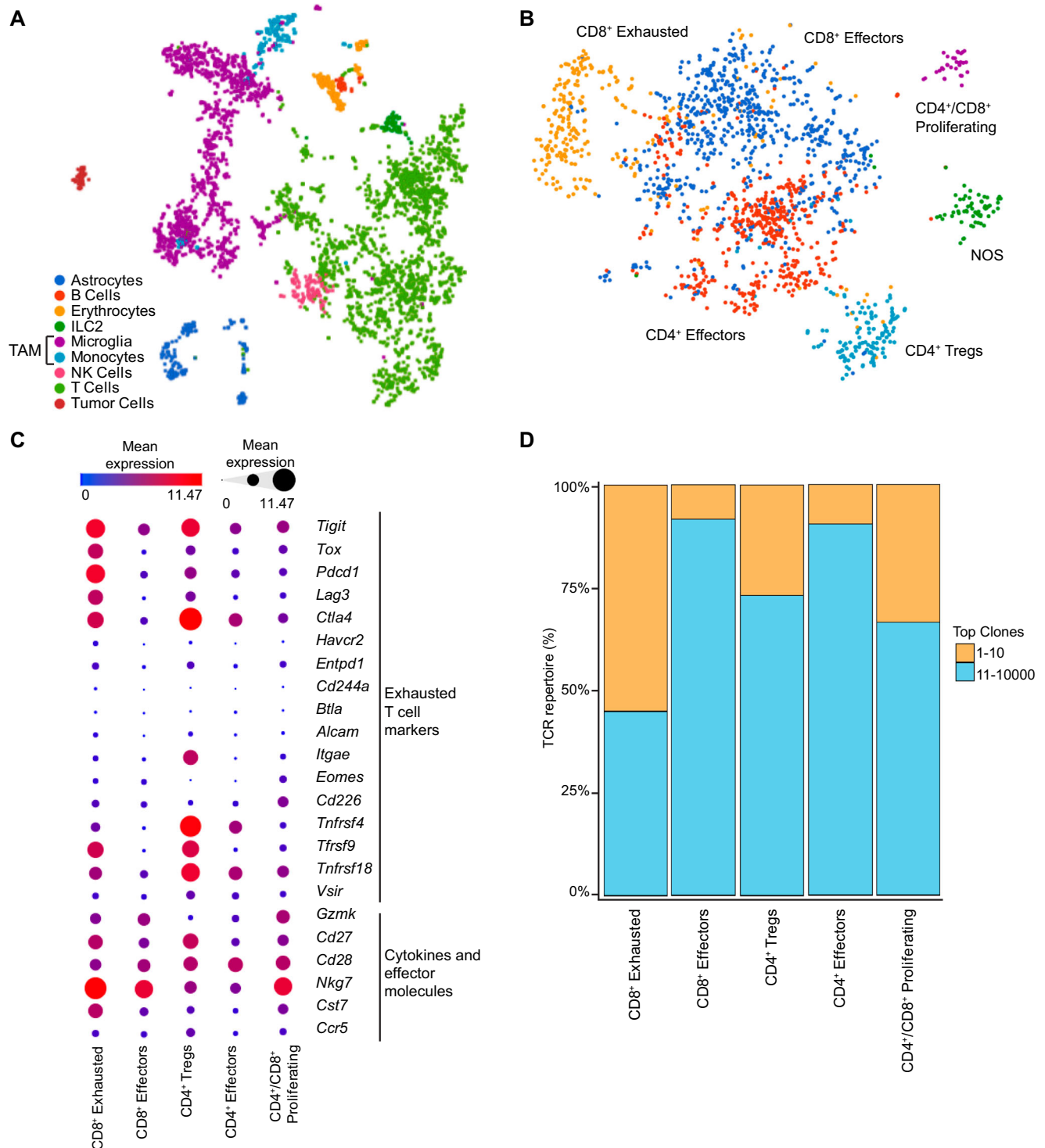


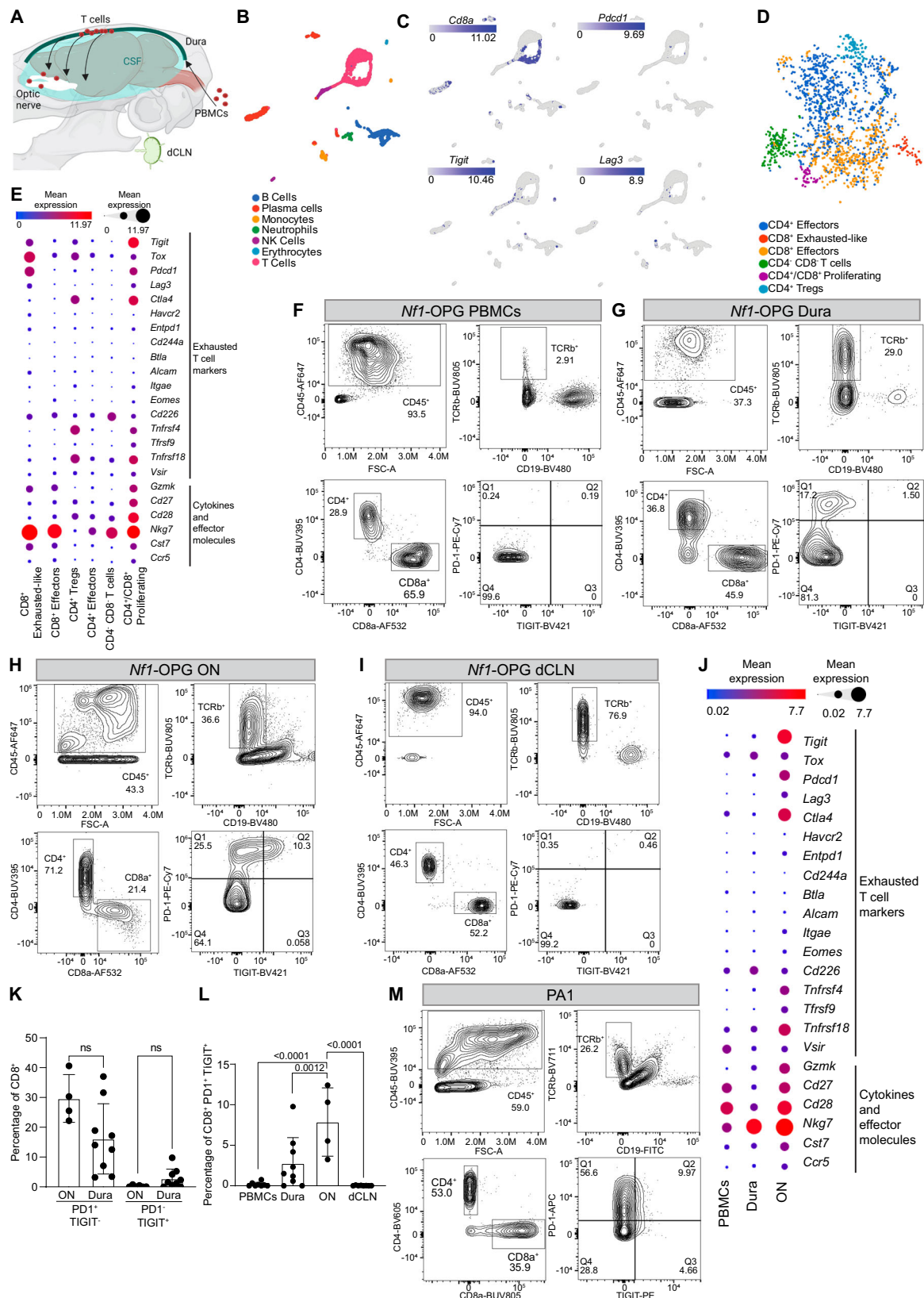
Fig. 2 | CD8⁺ exhausted T cells are present in the optic nerve of *Nf1*-OPG mice. **A** t-SNE visualization of scRNAseq data of optic nerves collected from 12-week-old *Nf1*-OPG mice, based on cell type; $n = 10$ pooled mice. Microglia and monocytes constitute tumor associated monocytes (TAM). **B** t-SNE visualization of the T cell populations from 12-week-old *Nf1*-OPG mouse optic nerves, color-coded by T cell

type. NOS, not otherwise specified. **C** Dot plot showing the genes used to identify CD8⁺ exhausted T cells in 12-week-old *Nf1*-OPG mouse optic nerves. **D** Stacked bar plot representing the barcode frequency of the top clones in the different T cell populations in 12-week-old *Nf1*-OPG mouse optic nerves. The graph is color coded to show the 1–10 clones and 11–10,000 clones.

Fig. 6D, E). In this regard, optic nerve volumes and TAM content are similar in *Nf1*^{+/−} and *Nf1*-OPG mice, where they reflect the impact of a heterozygous *Nf1* mutation, rather than features of an optic glioma in mice³⁵.

Since children with NF1-OPG experience vision loss as a result of tumor-induced retinal ganglion cell (RGC) content and axon

thickness^{36,37}, we assessed the number of retinal ganglion cells (RGCs) and the retinal nerve fiber layer (RNFL) thickness in *Nf1*-OPG mice following ICI treatment, as previously reported³⁷. While there was no improvement in RGC content, the RNFL thickness was restored to wild type levels following combined α -PD1 + TIGIT antibody treatment (Supplementary Fig. 6F).



Since CTLA4 is expressed at higher levels than TIGIT in human PA CD8⁺ exhausted T cells, we also treated *Nf1*-OPG mice with α -CTLA4 antibodies (Fig. 1E, I). Following α -CTLA4 antibody treatment (Supplementary Fig. 7A), we observed a 90% decrease in tumor proliferation, as well as a reduction in the number of CD8⁺ T cells and optic nerve volume (Supplementary Fig. 7B-D). In

contrast, the percentage of Iba1⁺ cells was not changed (Supplementary Fig. 7E).

As the CD8⁺ exhausted T cells express *Ccl4*, which is necessary for immune support of *Nf1*-OPG growth, we assayed *Ccl4* mRNA levels by RT-qPCR in the optic nerve. Reduced *Ccl4* expression was only observed after combination antibody therapy (75% decrease,

Fig. 3 | PD1⁺ TIGIT⁺ CD8⁺ exhausted T cells are enriched in the tumors from *Nf1*-OPG mice. **A** Schematic representation of T cell circulation from the blood through the dura meninges (dura), optic nerve (ON), and draining deep cervical lymph nodes (dCLN). Created in BioRender. Chatterjee, J. (2023) BioRender.com/f03c341. **B** t-SNE visualization of scRNAseq data from 12-week-old *Nf1*-OPG mice peripheral blood mononuclear cells (PBMCs), based on cell type; $n = 10$ pooled mice. **C** t-SNE visualization of scRNAseq data from 12-week-old *Nf1*-OPG PBMCs, color-coded by gene expression (*Cd8a*, *Pdcd1*, *Tigrit*, *Lag3*). **D** t-SNE visualization of the T cell populations from 12-week-old *Nf1*-OPG mouse meningeal dura, color-coded by T cell type, $n = 10$ pooled mice. **E** Dot plot showing the genes used to identify CD8⁺ exhausted T cells in the 12-week-old *Nf1*-OPG mouse meningeal dura scRNAseq dataset. Representative gating strategy for flow cytometry of 12-week-old PMBC T cells ($n = 9$ mice) (**F**), meningeal dura ($n = 9$ mice) (**G**), optic nerve ($n = 4$, 3 pooled optic nerves per sample) (**H**), and deep cervical lymph nodes dura ($n = 9$ mice) (**I**). **J** Dot plot showing the genes used to identify CD8⁺ exhausted T cells in 12-week-old

Nf1-OPG mouse optic nerves (corresponds to the dataset shown in Fig. 2; $n = 10$ pooled mice), meningeal dura (corresponds to the dataset shown in (D); $n = 10$ pooled mice), and PBMC (corresponds to the dataset shown in (B); $n = 10$ pooled mice) scRNAseq datasets. **K** Graph representing the percentages of CD8⁺/PD1⁺ and CD8⁺/TIGIT⁺ cells in the optic nerves (ON) and dura of 12-week-old *Nf1*-OPG mice (ON, $n = 4$, 3 pooled optic nerves per sample; dura, $n = 9$ mice). Data are represented as mean \pm SD. A one-way ANOVA test was performed followed by a Dunnett's post-test correction. Exact P values are indicated. **L** Graph comparing the percentages of CD8⁺/PD1⁺/TIGIT⁺ cells in the PBMCs, dura, optic nerve (ON), and dCLN, of 12-week-old *Nf1*-OPG mice (PBMCs, $n = 8$ mice; dura, $n = 9$ mice; ON, $n = 4$, 3 pooled optic nerves per sample; dCLN, $n = 8$ mice). Data are shown as mean \pm SD. A one-way ANOVA test was performed followed by a Holm-Šidák post-test correction. Exact P values are included. **M** Representative gating strategy for flow cytometry of one representative human PA1 ($n = 1$; corresponds to PA1 sample in Fig. 1F).

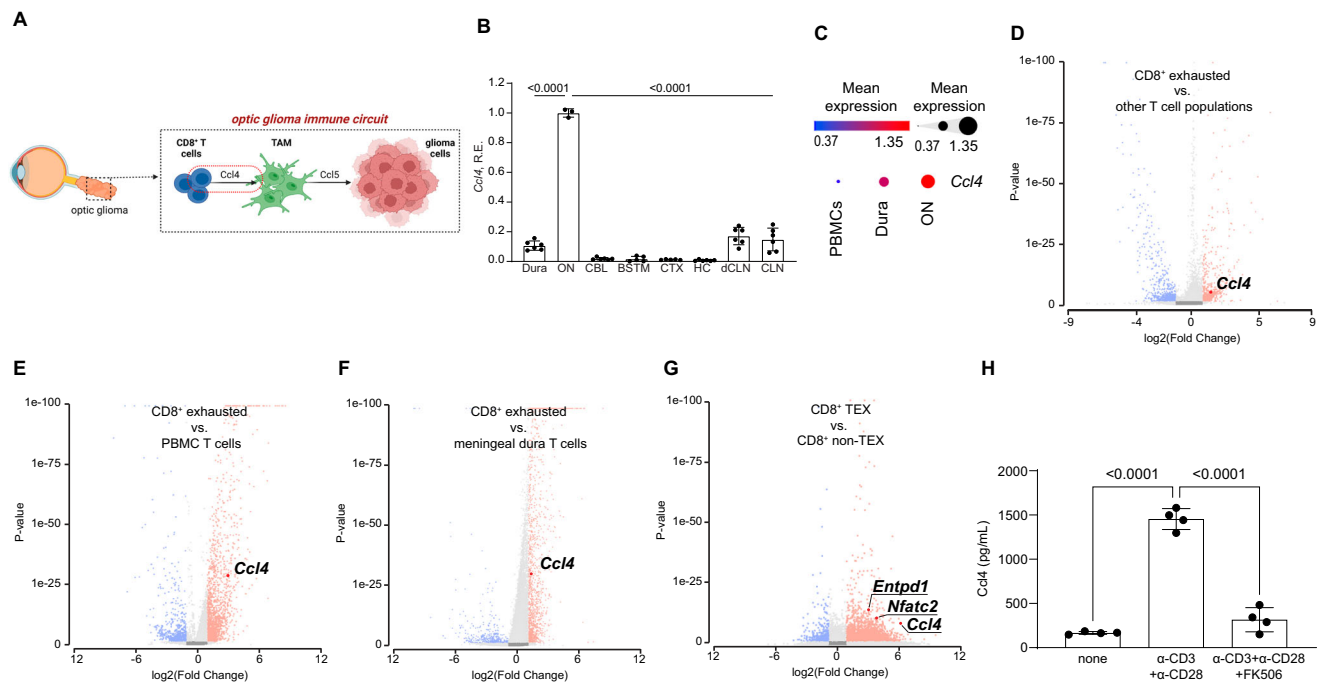
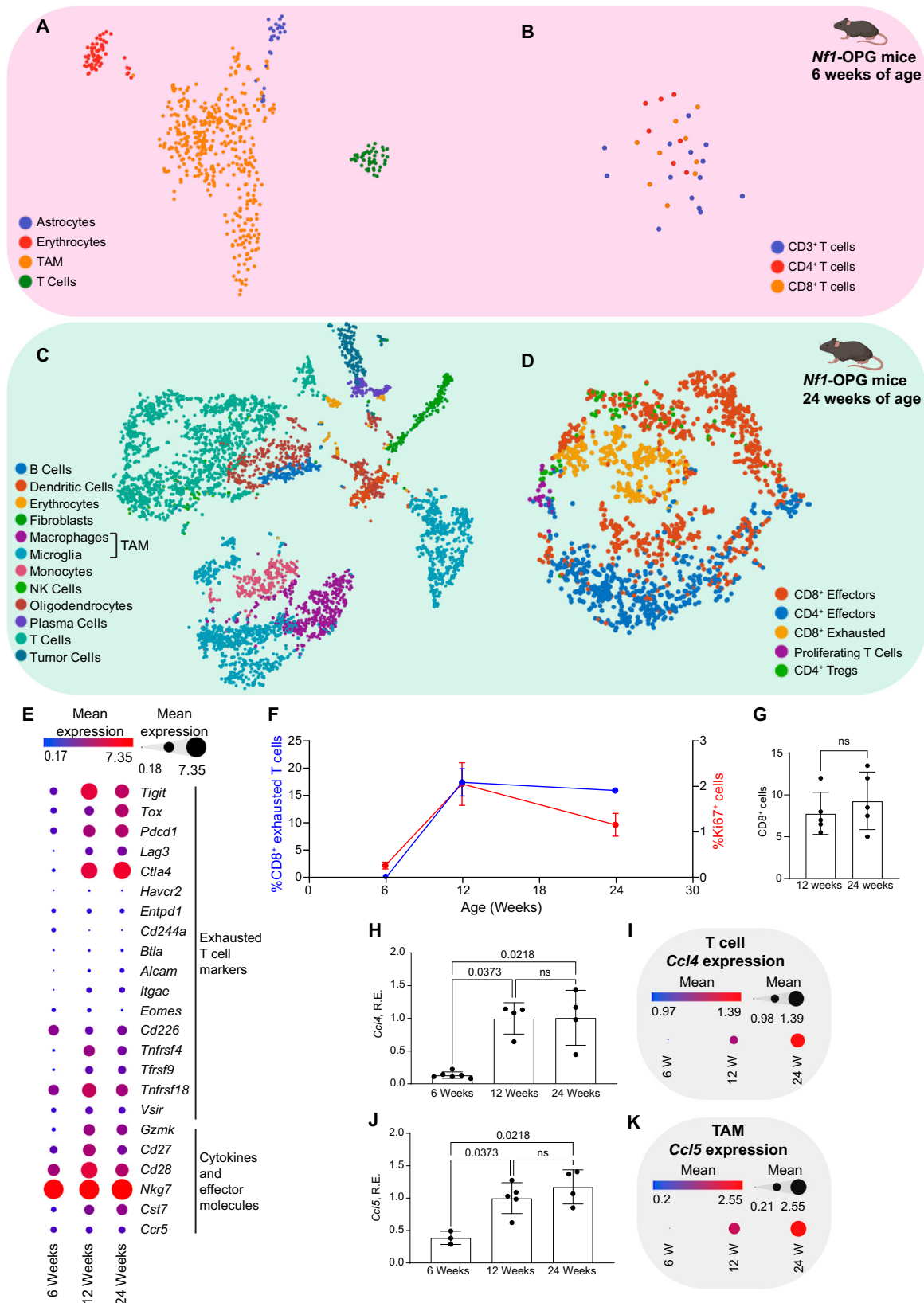


Fig. 4 | CD8⁺ exhausted T cells express *Ccl4*. **A** Schematic representation of the optic glioma immune circuit. Created in BioRender. Chatterjee, J. (2024) BioRender.com/e28x983. **B** *Ccl4* expression in the dura, optic nerve (ON), cerebellum (CBL), brainstem (BSTM), cortex (CTX), hippocampus (HC), deep cervical lymph nodes (dCLN), and superficial cervical lymph nodes (CLN) of 12-week-old *Nf1*-OPG mice, following normalization to the optic nerve. Data are represented as mean \pm SD. (dura, $n = 6$ mice; ON, $n = 3$, 2 pooled optic nerves per sample; CBL, $n = 6$ mice; BSTM, $n = 5$ mice; CTX, $n = 5$ mice; HC, $n = 6$ mice; dCLN, $n = 6$ mice; CLN, $n = 6$ mice). A one-way ANOVA test was performed followed by a Holm-Šidák post-test correction. Exact P values are included. **C** Dot plot showing *Ccl4* expression from 12-week-old *Nf1*-OPG mouse optic nerves (corresponds to the dataset shown in Fig. 2; $n = 10$ pooled mice), meningeal dura (corresponds to the dataset shown in Fig. 3D; $n = 10$ pooled mice), and PBMC (corresponds to the dataset shown in Fig. 3B; $n = 10$ pooled mice) scRNAseq datasets. **D** Volcano plot showing fold change and P value comparing CD8⁺ exhausted T cells and the other T cell populations in the optic nerves of 12-week-old *Nf1*-OPG mice (corresponds to the dataset shown in Fig. 2; $n = 10$ pooled mice). Upregulated genes in red, downregulated genes in blue. Differential analyses were performed using gene specific analysis (GSA). **E** Volcano plot showing fold change and P value comparing CD8⁺ exhausted T cells in the optic nerves (corresponds to the dataset shown in Fig. 2; $n = 10$ pooled mice) and PMBC T cells of 12-week-old *Nf1*-OPG mice (corresponds to the dataset shown in Fig. 3B;

$n = 10$ pooled mice). Upregulated genes in red, downregulated genes in blue. Differential analyses were performed using gene specific analysis (GSA). **F** Volcano plot showing fold change and P value comparing CD8⁺ exhausted T cells in the optic nerves (corresponds to the dataset shown in Fig. 2, Supplementary Fig. 2; $n = 10$ pooled mice in each dataset) and T cells from the dura of 12-week-old *Nf1*-OPG mice (corresponds to the dataset shown in Fig. 3D; $n = 10$ pooled mice). Upregulated genes in red, downregulated genes in blue. Differential analyses were performed using gene specific analysis (GSA). **G** Volcano plot showing fold change and P value comparing CD8⁺ TEX in the optic nerves (corresponds to the dataset shown in Fig. 2; $n = 10$ pooled mice), and to the dataset shown in Supplementary Fig. 2; $n = 10$ pooled mice) and CD8⁺ non-TEX T cells of 12-week-old *Nf1*-OPG mice (corresponds to the dataset shown in Fig. 2; $n = 10$ pooled mice, and to the dataset shown in Supplementary Fig. 2; $n = 10$ pooled mice). Upregulated genes in red, downregulated genes in blue. Differential analyses were performed using gene specific analysis (GSA). **H** Graph showing levels of secreted *Ccl4* in the TCM by ELISA of unstimulated and CD8⁺ exhausted T cells (α -CD3+ α -CD28 antibody stimulated) with and without FK506 treatment (none, $n = 4$; α -CD3+ α -CD28, $n = 4$; α -CD3+ α -CD28 + FK506, $n = 4$). A one-way ANOVA test was performed followed by a Holm-Šidák post-test correction. Data are represented as mean \pm SD. Exact P values are indicated.

$P = 0.0077$) (Fig. 7B). Since T cell *Ccl4* induces TAM expression of *Ccl5* in *Nf1*-OPG mice, we measured *Ccl5* levels. Similar to *Ccl4*, *Ccl5* expression was only reduced following combination α -PD1/ α -TIGIT antibody therapy (80% decrease, $P = 0.0179$) (Fig. 7C). These results

demonstrate that combination α -PD1/ α -TIGIT treatment reduces tumor cell proliferation by abrogating *Ccl4*/*Ccl5* stromal support but does not explain the tumor suppressive effect of α -PD1 antibody therapy alone.



To identify this PD1-mediated *Ccl4*-independent CD8⁺ T cell-dependent mechanism, we hypothesized that CD8⁺ T cells might produce a growth factor that directly regulates tumor cell growth. First, using CD8⁺ T cell conditioned medium (TCM) from exhausted CD8⁺ T cells (α -CD3 and α -CD28 antibody stimulated), we found that TCM from these CD8⁺ exhausted T cells (α -CD3 and α -CD28 antibody

treated) increased optic glioma tumor cell (o-GTC) proliferation (% Ki67⁺ cells) by two-fold relative to non-exhausted (unstimulated) CD8⁺ TCM in vitro (Fig. 7D). Second, we leveraged our *Nf1*-OPG optic glioma scRNAseq data to identify a potential soluble factor enriched in CD8⁺ PD1⁺ T cells relative to CD8⁺ PD1^{neg} T cells. We found that *Tgfb1* expression was increased (fold change = 2.03, $P = 3.89 \times 10^{-9}$) in CD8⁺

Fig. 5 | Presence of CD8⁺ exhausted T cells mirrors optic glioma growth and *Ccl4/Ccl5* expression. **A** t-SNE visualization of scRNAseq data from optic nerves of 6-week-old *Nf1*-OPG mice, based on cell type, $n = 10$ pooled mice. **B** t-SNE visualization of the T cell populations from 6-week-old *Nf1*-OPG mice, color-coded by T cell type. Created in BioRender. Chatterjee, J. (2023) BioRender.com/p15a720. **C** t-SNE visualization of scRNAseq data from optic nerves of 24-week-old *Nf1*-OPG mice, based on cell type, $n = 10$ pooled mice. Microglia and monocytes constitute tumor associated monocytes (TAM). **D** t-SNE visualization of the T cell populations from 24-week-old *Nf1*-OPG mice, color-coded by T cell type. Created in BioRender. Chatterjee, J. (2023) BioRender.com/p15a720. **E** Dot plot showing genes used to identify CD8⁺ exhausted T cells in 6- (corresponds to the dataset shown in Fig. 5A; $n = 10$ pooled mice), 12- (corresponds to the datasets shown in Fig. 2 and Supplementary Fig. 2; $n = 10$ pooled mice in each dataset), and 24-week-old *Nf1*-OPG mouse optic nerves (corresponds to the dataset shown in (C); $n = 10$ pooled mice). **F** Graph showing changes in the percentage of CD8⁺ exhausted T cells (blue) in 6-week-old (corresponds to the dataset shown in (A); $n = 10$ pooled mice), 12-week-old (corresponds to the datasets shown in Fig. 2 and Supplementary Fig. 2; $n = 10$ pooled mice in each dataset), and 24-week-old (corresponds to the dataset shown in (C); $n = 10$ pooled mice) *Nf1*-OPG mice and proliferating (Ki67⁺ cells; red) tumor cells over time (6 weeks, $n = 5$ mice; 12 weeks, $n = 4$ mice; 24 weeks, $n = 4$ mice). Data are represented as mean \pm SD. **G** Quantification CD8⁺ T cells in the optic nerves of *Nf1*-OPG mice at 12 and 24 weeks of age (12 weeks, $n = 5$ mice; 24 weeks, $n = 5$ mice). Data are represented as mean \pm SD. To evaluate statistical differences, a two-tailed

non-parametric Mann-Whitney test was performed. Exact P values are indicated. ns, not significant. **H** *Ccl4* RNA expression in the optic nerves of 6-week-old, 12-week-old, and 24-week-old *Nf1*-OPG mice. Data are represented relative to the 12-week-old group (6-week-old mice, $n = 6$, 2 pooled optic nerves per sample; 12-week-old mice, $n = 4$, 2 pooled optic nerves per sample; 24-week-old mice, $n = 4$, 2 pooled optic nerves per sample). Data are represented as mean \pm SD. A one-way ANOVA test was performed followed by a Dunnett's post-test correction. Exact P values are indicated. ns, not significant. **I** Dot plot showing *Ccl4* expression in T cells from optic nerves of 6-week-old (6 W; corresponds to the dataset shown in (A); $n = 10$ pooled mice), 12-week-old (12 W) (corresponds to the datasets shown in Fig. 2 and Supplementary Fig. 2; $n = 10$ pooled mice in each dataset), and 24-week-old (24 W) (corresponds to the dataset shown in (C); $n = 10$ pooled mice) *Nf1*-OPG mice. **J** *Ccl5* RNA expression in the optic nerves of 6-week-old, 12-week-old, and 24-week-old *Nf1*-OPG mice. Data are represented relative to the 12-week-old group (6-week-old mice, $n = 3$, 2 pooled optic nerves per sample; 12-week-old mice, $n = 5$, 2 pooled optic nerves per sample; 24-week-old mice, $n = 4$, 2 pooled optic nerves per sample). Data are represented as mean \pm SD. A one-way ANOVA test was performed followed by a Dunnett's post-test correction. Exact P values are indicated. ns, not significant. **K** Dot plot showing *Ccl5* expression in TAM from the optic nerves of 6-week-old (6 W; corresponds to the dataset shown in (A); $n = 10$ pooled mice), 12-week-old (12 W) (corresponds to the datasets shown in Fig. 2 and Supplementary Fig. 2; $n = 10$ pooled mice in each dataset), and 24-week-old (24 W) (corresponds to the dataset shown in (C); $n = 10$ pooled mice) *Nf1*-OPG mice.

PD1⁺ T cells relative to other CD8⁺ PD1^{neg} T cell populations (Fig. 7E). scRNAseq of optic nerves from 6, 12, and 24-week-old *Nf1*-OPG mice (Supplementary Fig. 8A) revealed higher expression levels of *Tgfb1* at 12 and 24 weeks of age relative to 6 weeks of age, coinciding with the infiltration of CD8⁺ T cells in these tumors. Third, we demonstrated that TGF β expression is increased in stimulated CD8⁺ T cells (α -CD3+ α -CD28 antibody treatment) compared to unstimulated CD8⁺ T cells using RT-qPCR (fold change = 2.3, $P = 0.0286$) and ELISA (fold change = 4.9, $P = 0.0286$) (Supplementary Fig. 8B, Fig. 7F). Fourth, the addition of TGF β at the concentration detected in the TCM of CD8⁺ T cells following α -CD3+ α -CD28 antibody treatment in vitro increased optic glioma tumor cell (o-GTC) proliferation (fold change = 1.62, $P = 0.0043$, Supplementary Fig. 8C). Fifth, *Tgfb1* expression was only reduced (57% reduction) in *Nf1*-OPG mice treated with α -PD1, but not α -TIGIT, antibodies alone (Fig. 7G). Sixth, to confirm that TGF β is a stromal mitogen critical for *Nf1*-OPG growth, *Nf1*-OPG mice were treated with α -TGF β neutralizing antibodies from 12 to 16 weeks of age (Fig. 7H). Following α -TGF β antibody treatment in vivo, optic glioma proliferation (Ki67⁺ cells) and CD8⁺ T cell numbers were reduced and the RNFL was increased to wild type levels (Fig. 7I, J, Supplementary Fig. 8D–F). As before, no changes were observed in optic nerve volume, TAM content, or RGC number (Supplementary Fig. 8D–E). Taken together, these data reveal a CD8⁺ PD1⁺ T cell-TGF β -dependent mechanism additionally important for governing *Nf1*-OPG tumor growth (Fig. 7K).

In contrast to previous studies in which ICI therapy results in increased CD8⁺ T cell-mediated tumor cell death (killing)^{38,39}, we observed no increase in tumor apoptosis (Supplementary Fig. 9A), ferroptosis (Supplementary Fig. 9B), or expression of genes associated with T cell-mediated cytotoxicity (Supplementary Fig. 9C). Additionally, there was also no increase in o-GTC death following the addition of TCM from exhausted CD8⁺ T cells (stimulated with α -CD3 and α -CD28 antibodies) in vitro (Supplementary Fig. 9D).

Discussion

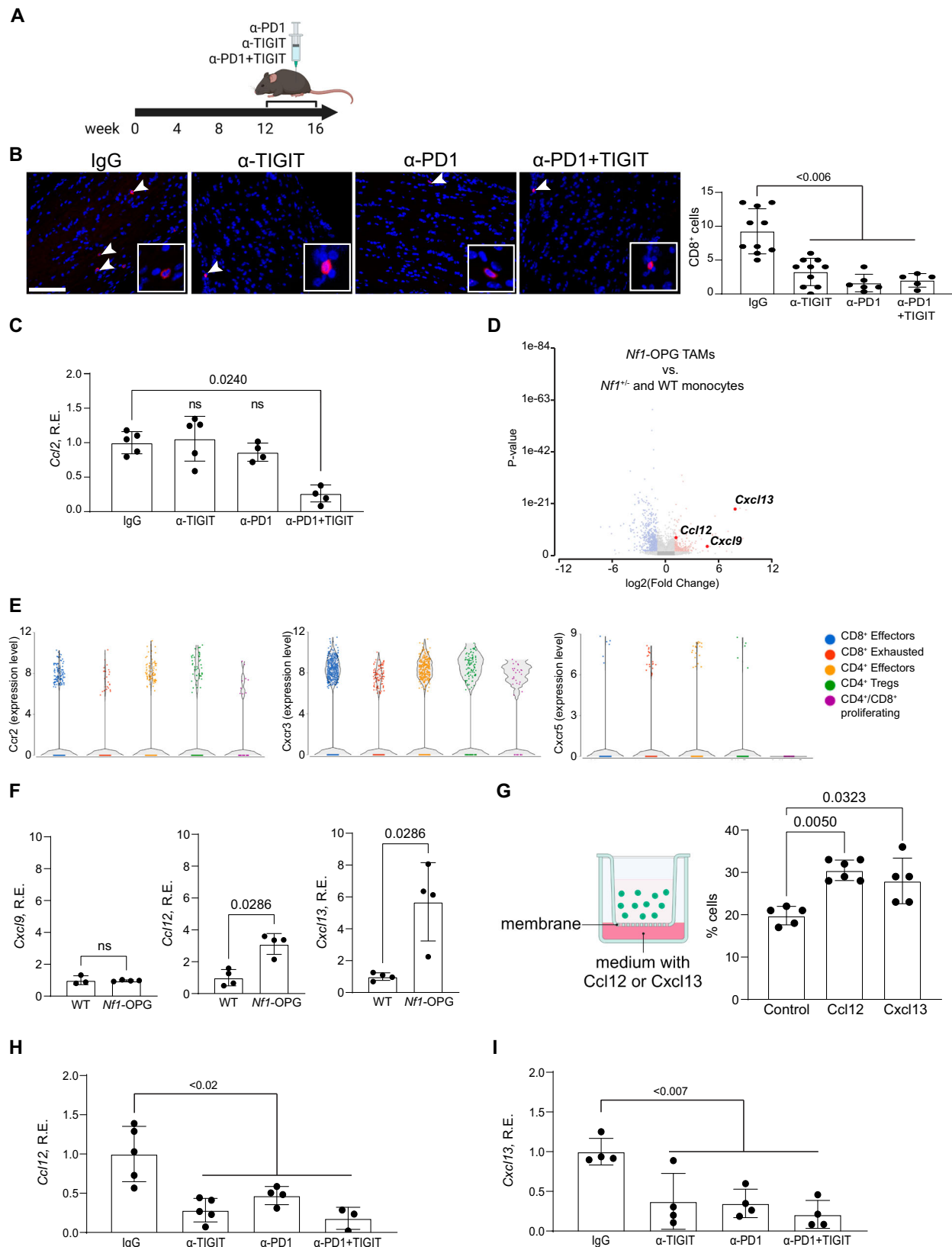
While lymphoid cells constitute a minor population of non-neoplastic cells within the brain tumor microenvironment, studies over the past decade have revealed important contributions for T cells in tumor maintenance and progression. Combining several converging and complementary strategies, we identify a specialized population of CD8⁺ exhausted T cells enriched in human LGGs relative to their malignant counterparts, which, in experimental LGG mouse models, is

critical for stromal support of LGG growth. These observations raise several important points relevant to T cell control of brain tumor biology.

First, while there are numerous reports of CD8⁺ exhausted T cells in malignant tumors, few studies have focused on low-grade tumors⁴⁰. While CD8⁺ T cells are found in benign schwannomas, PD1⁺TIM3⁺ CD8⁺ exhausted T cells were enriched only in malignant schwannomas⁴¹. Similarly, high-grade pancreatic cancers are highly infiltrated by CD8⁺ exhausted T cells, whereas their low-grade counterparts harbor a high ratio of activated CD8⁺ effector T cells⁴². In contrast, we demonstrate that CD8⁺ exhausted T cells are enriched in pediatric LGGs relative to both pediatric and adult HGGs. It should be noted that, unlike HGGs, PAs in children are typically chronic disorders with limited mortality and tend to behave in an indolent manner⁴³. To this end, the majority of NF1-associated PAs (OPGs) grow during early childhood, with rare examples of spontaneous tumor regression reported⁴⁴. For these reasons, we postulate that this unique population of CD8⁺ exhausted T cells functions in a unique manner in the setting of childhood LGG.

Second, the CD8⁺ exhausted T cells do not appear to function as cytotoxic effectors or inert bystanders, as described for some malignant cancers^{25,45}. In this regard, α -PD1, α -TIGIT, or combined α -PD1/ α -TIGIT ICI therapy did not result in tumor cell death by apoptosis or ferroptosis, nor was there increased expression of effector CD8⁺ T cell cytotoxic genes typically induced following successful PD1 treatment of malignant cancers^{46–48}. Additionally, the PD1⁺/TIGIT⁺/CD39⁺ population of CD8⁺ T cells was restricted to the tumor in *Nf1*-OPG mice, where specific cellular interactions allow for their enrichment and/or expansion. In this regard, there was a higher expression of PD1 (*CD274*) and TIGIT (*Pvr* and *Nectin2*) ligands in the optic nerve relative to the meningeal dura by scRNAseq and RT-qPCR (Supplementary Fig. 10A, B).

Third, to exclude the possibility that the anti-tumor effects observed following α -PD1 or α -PD1/TIGIT antibody treatments reflected non-specific targeting of multiple cell populations, we examined expression of classical exhaustion genes in the scRNAseq datasets (Supplementary Fig. 6G, H). We found that TAM have low *Pdcd1* (PD1) and no *Tigit* expression, NK cells express *Tigit*, but not *Pdcd1*, and CD4⁺ Tregs express both *Pdcd1* and *Tigit*. While all three of these stromal cell types have been shown to regulate tumor growth^{49–51} in the context of *Nf1*-OPG tumors, neither TAM (Supplementary Fig. 4F), NK cells (Supplementary Fig. 4K) or CD4⁺ Tregs (Supplementary Fig. 4C, D) were responsible for observed increase in *Ccl4* expression. In addition,



antibody-mediated NK cell depletion had no effect on *Nf1*-OPG proliferation (Supplementary Fig. 11A–C). For these reasons, the tumor-suppressing effect of α-PD1/TIGIT antibody treatment is most likely due to the targeting of CD8⁺ exhausted T cells.

Fourth, in addition to Ccl4-mediated TAM Ccl5 production, we elucidated a second CD8⁺ exhausted T cell-mediated *Nf1*-OPG growth

regulatory mechanism. While prior reports have shown that TGFβ can induce tumor cell proliferation and migration in other cancers^{52,53}, this growth factor can also create an immunosuppressive environment causing CD8⁺ T cell anergy and suppression of cytotoxic function⁵⁴. In contrast, we demonstrate, that the CD8⁺ exhausted T cells are active participants in tumor growth. As such, CD8⁺ exhausted T cells also

Fig. 6 | Anti-PD1⁺/TIGIT⁺ ICI treatment reduces CD8⁺ T cell infiltration by decreasing TAM-mediated Ccl12 and Cxcl13 chemoattraction. **A** Schematic representation of the anti-PD1 (α-PD1), anti-TIGIT (α-TIGIT), and combined (α-PD1 + TIGIT) antibody treatments. *Nfl*-OPG mice were treated (200 μg/dose/ i.p., twice per week) from 12 to 16 weeks of age, and tissues were analyzed at 16 weeks. The control group was injected with anti-IgG isotype control antibodies. Created in BioRender. Chatterjee, J. (2024) BioRender.com/r98n914. **B** Immunohistochemistry and quantification CD8⁺ T cells in the entire optic nerve (IgG, *n* = 10 mice; α-TIGIT, *n* = 10 mice; α-PD1, *n* = 6 mice; α-PD1 + TIGIT, *n* = 5 mice). Data are represented as mean ± SD. A one-way ANOVA test was performed followed by a Dunnett's post-test correction. Exact *P* values are indicated (α-TIGIT, *P* = 0.0054; α-PD1, *P* = 0.0003; α-PD1 + TIGIT, *P* = 0.0032). Scale bar, 200 μm. **C** *Ccl2* RNA expression in the optic nerves of *Nfl*-OPG mice treated with IgG, α-TIGIT, α-PD1 or a combination of α-PD1 and α-TIGIT antibodies. Data are represented relative to the IgG control group (IgG, *n* = 5, 2 pooled optic nerves per sample; α-TIGIT *n* = 5, 2 pooled optic nerves per sample; α-PD1, *n* = 4, 2 pooled optic nerves per sample; α-PD1 + TIGIT, *n* = 4, 2 pooled optic nerves per sample). Data are represented as mean ± SD. A one-way ANOVA test was performed followed by a Dunnett's post-test correction. Exact *P* values are indicated. **D** Volcano plot showing fold change and *P* value comparing *Nfl*-OPG TAM to *Nfl*^{+/+} and WT monocytes in the optic nerves of 12-week-old mice. Upregulated genes in red, downregulated genes in blue. Differential analyses were performed using gene specific analysis (GSA). **E** *Ccr2*, *Cxcr3*, and *Cxcr5* expression in T cell populations from 12-week-old *Nfl*-OPG mouse optic nerves, color-coded by T cell type. **F** *Cxcl9*, *Ccl12*, and *Cxcl13* RNA expression in the optic nerves of 12-week-old WT and *Nfl*-OPG mice. Data are represented relative to the WT group (*Cxcl9*; WT *n* = 3, 2 pooled optic nerves per sample; *Nfl*-OPG *n* = 4, 2 pooled optic nerves per

sample; *Ccl12*; WT *n* = 4, 2 pooled optic nerves per sample; *Nfl*-OPG *n* = 4, 2 pooled optic nerves per sample; *Cxcl13*; WT *n* = 4, 2 pooled optic nerves per sample; *Nfl*-OPG *n* = 4, 2 pooled optic nerves per sample). Data are represented as mean ± SD. To evaluate statistical differences, a two-tailed non-parametric Mann–Whitney test was performed. Exact *P* values are indicated. ns, not significant. **G** Graph showing the percentage of migrated *Nfl*^{+/+} CD8⁺ T cells treated with medium (Control) (*n* = 5), *Ccl12* (*n* = 6), or *Cxcl13* (*n* = 5). Data are represented as mean ± SD. A one-way ANOVA test was performed followed by a Dunnett's post-test correction. Exact *P* values are indicated. Created in BioRender. Chatterjee, J. (2024) BioRender.com/r98n914.

H *Ccl12* RNA expression in the optic nerves of *Nfl*-OPG mice treated with IgG, α-TIGIT, α-PD1 or a combination of α-PD1 and α-TIGIT antibodies. Data are represented relative to the IgG control group (IgG, *n* = 5, 2 pooled optic nerves per sample; α-TIGIT *n* = 5, 2 pooled optic nerves per sample; α-PD1, *n* = 4, 2 pooled optic nerves per sample; α-PD1 + TIGIT, *n* = 3, 2 pooled optic nerves per sample). Data are represented as mean ± SD. A one-way ANOVA test was performed followed by a Tukey's post-test correction. Exact *P* values are indicated (α-TIGIT, *P* = 0.0012; α-PD1, *P* = 0.0187; α-PD1 + TIGIT, *P* = 0.0013). **I** *Cxcl13* RNA expression in the optic nerves of *Nfl*-OPG mice treated with IgG, α-TIGIT, α-PD1 or a combination of α-PD1 and α-TIGIT antibodies. Data are represented relative to the IgG control group (IgG, *n* = 4, 2 pooled optic nerves per sample; α-TIGIT *n* = 4, 2 pooled optic nerves per sample; α-PD1, *n* = 4, 2 pooled optic nerves per sample; α-PD1 + TIGIT, *n* = 4, 2 pooled optic nerves per sample). Data are represented as mean ± SD. A one-way ANOVA test was performed followed by a Tukey's post test correction. Exact *P* values are indicated (α-TIGIT, *P* = 0.0003; α-PD1, *P* = 0.0007; α-PD1 + TIGIT, *P* = 0.0001).

produce TGFβ, which is *sufficient* to increase α-GTC growth in vitro, and α-PD1/TIGIT antibody treatment reduces *Tgfb1* expression. Moreover, α-TGFβ antibody treatment attenuates *Nfl*-OPG growth in vivo, establishing that this cytokine is *necessary* for tumor proliferation. Relevant to future therapeutic application, the encouraging successes observed with the use of TGFβ inhibitors in combination with standard therapies for malignant glioma (HGG) and multiple myeloma^{55,56} provides support for the use of TGFβ inhibitors, including TGFβ-directed small molecule inhibitors, chimeric monoclonal antibodies, ligand traps, and vaccines⁵⁷, as adjuvant therapies to improve ICI responses.

Fifth, in addition to discovering another growth regulatory mechanism, we identified other chemokines responsible for CD8⁺ T cell tumor infiltration. As such, we previously showed that *Ccl2* was produced by optic glioma tumor cells, which attracts CD8⁺ T cells in a *Ccr4*-dependent manner³². Using an unbiased approach, we identified two chemoattractants, *Ccl12* and *Cxcl13*, that are responsible for the recruitment of CD8⁺ T cells. While the mechanism for TAM production of *Cxcl13* and *Ccl12* in the *Nfl*-OPG model is unknown, we are actively investigating the role of cytokine/chemokines and other factors in TAM *Cxcl13*/*Ccl12* regulation. Although *Ccl12* is not expressed in humans, CXCL13 has been shown to mediate T cell attraction in other human cancers^{58,59}. In this regard, CXCL13 is produced by macrophages in some cancers⁶⁰ and was originally described as a B cell chemoattractant⁶¹. Moreover, it has been postulated to represent a potential marker to predict the response to ICI therapy⁶². Future studies will be required to determine whether CXCL13 could serve as a target for LGG therapy or a marker of disease progression.

Taken together, we report a new role for CD8⁺ exhausted T cells in LGGs where they function as part of two distinct immune paracrine stromal circuits that support tumor growth. Further investigation of this unique CD8⁺ T cell population may reveal additional molecular vulnerabilities that could lead to adjuvant immune-directed treatments for low-grade brain tumors in children.

Methods

All research is compliant with the relevant ethical bodies. All experiments were performed in compliance with active Animal Studies Committee protocols at the Washington University School of Medicine.

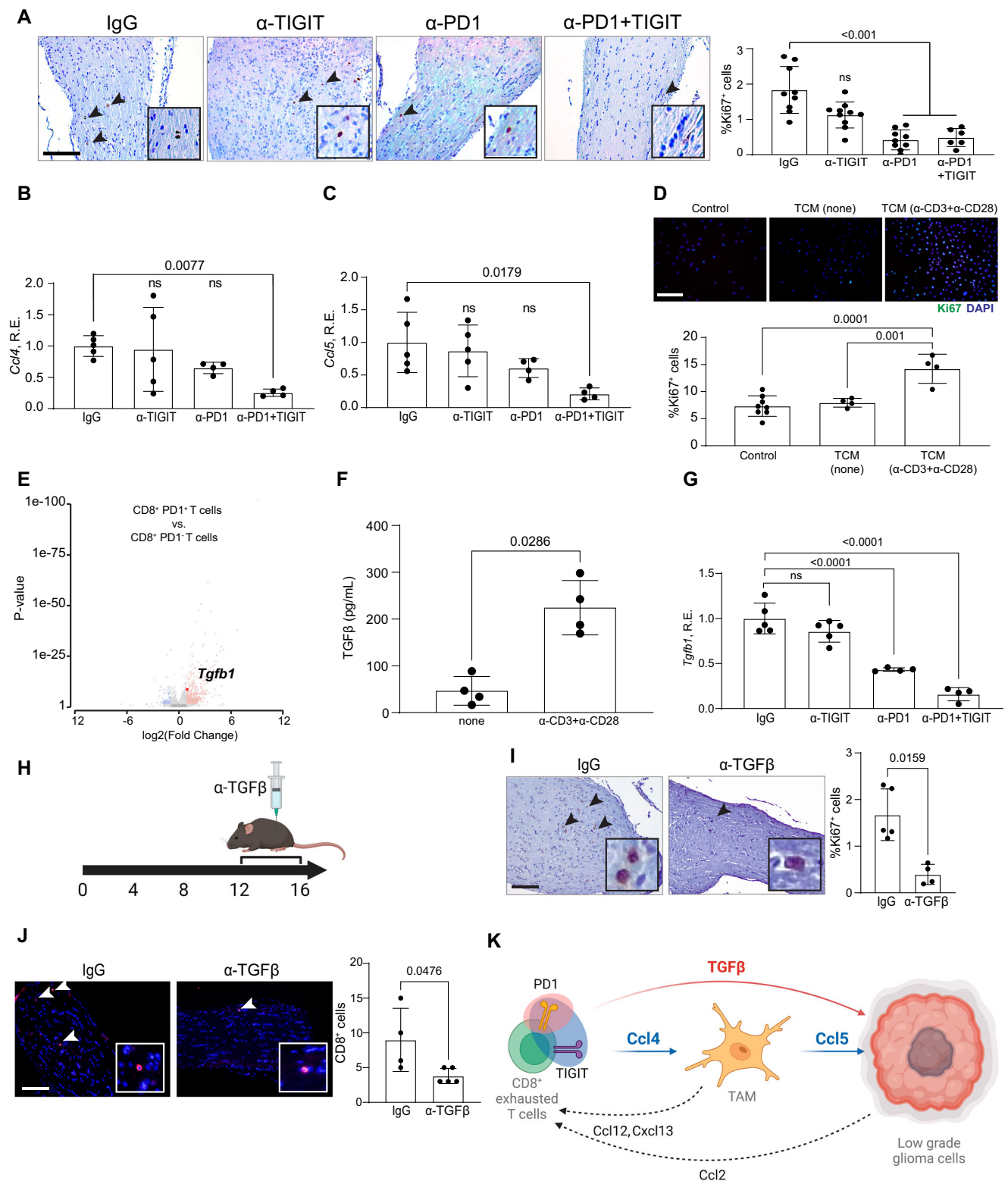
Mice

All experiments were performed according to the active Animal Studies Committee protocols at the Washington University School of Medicine (Washington University in St. Louis Institutional Animal Care and Use Committee). According to the ethics committee, any animals with compromised motion/eating habits or an unhealthy appearance are euthanized. No animals were euthanized due to their tumor burden or as a result of the treatments performed in this study. Mice harboring (1) a neomycin cassette insertion in exon 31 (*Nfl*±) with GFAP-Cre-mediated *Nfl* loss in neuroglial progenitors (*Nfl*^{fllox/neo}; GFAP-Cre, *Nfl*-OPG mice)¹⁷, (2) the patient-derived germline *Nfl* c.2041 C > T mutation^{30,31} with GFAP-Cre-mediated *Nfl* loss in neuroglial progenitors (*Nfl*^{fllox/R681X}; GFAP-Cre, *Nfl*^{681C} mice), and (3) the patient-derived germline *Nfl* c.5425 C > T mutation²¹ with GFAP-Cre-mediated *Nfl* loss in neuroglial progenitors (*Nfl*^{fllox/R1809C}; GFAP-Cre; *Nfl*^{1809C} mice) were used. *Nfl*^{+/+}, WT or *Nfl*^{fllox/fllox} mice were employed as controls. Mice of both sexes were randomly assigned to all experimental groups. All mice used in these experiments were maintained on a strict C57BL/6 background and were housed in a specific pathogen-free barrier facility with controlled temperature (21 °C), humidity (55%), light-dark cycles (12:12 h) and *ad libitum* access to food and water. Mice were euthanized by a barbiturate overdose using the Fatal Plus Pentobarbital solution at a dose of 86.6 mg/ml.

Optic nerve volume analysis

Dissected optic nerves were photographed using a Leica S9D Flexcam C3 microscope. The images were analyzed using ImageJ. Measurements at the chiasm 0 μm (D0), and at 150 μm (D150), 300 μm (D300), and 450 μm (D450) anterior to the chiasm were taken to generate optic nerve volume estimates, as previously reported¹⁹. The volumes for regions 1, 2, and 3 at the three 150 μm high-truncated cones were merged using the diameter (D0, D150, D300, and D450) values from each optic nerve measurement. Total optic nerve volumes were calculated according to this formula:

$$V1 = \frac{1}{12} \pi (D_0^2 + D_0 D_{150} + D_{150}^2) \quad (1)$$



In vivo mouse treatments

α -PD1 (BE0146; 200 μ g/dose, twice per week), α -TIGIT (BE0274; 200 μ g/dose, twice per week), combined α -PD1 and α -TIGIT (200 μ g + 200 μ g/dose, twice per week), α -CTLA4 (BE0131; 100 μ g/dose, twice per week), α -TGF β (BE0057; 200 μ g/dose, twice per week), α -Nk1.1 (BE0036; 200 μ g/dose, twice per week), or control IgG antibodies were administered to 12-week-old *Nf1*-OPG mice twice weekly i.p. for four consecutive weeks^{63–67}. All monoclonal antibodies and

their respective control IgG antibodies are listed in Supplementary Table 1.

Immunohistochemistry and immunofluorescence

Mice were euthanized and transcardially perfused with Ringer's solution, followed by 4% PFA. Optic nerves were harvested and embedded in paraffin, while eyes were collected and embedded in OCT. Serial 4- μ m-thick paraffin sections or 10- μ m-thick retinal cryosections were

Fig. 7 | Anti-PD1⁺/TIGIT⁺ ICI treatment reduces tumor cell proliferation through two distinct mechanisms. A Immunohistochemistry and quantification of proliferating (%Ki67⁺) cells in the optic nerves of *Nf1*-OPG mice (IgG, *n* = 9 mice; α -TIGIT, *n* = 10 mice; α -PD1, *n* = 9 mice; α -PD1 + TIGIT, *n* = 6 mice). Data are represented as mean \pm SD. A one-way ANOVA test was performed followed by a Dunnett's post-test correction. Exact *P* values are indicated (α -PD1, *P* < 0.0001; α -PD1 + TIGIT, *P* = 0.001). Scale bar, 200 μ m. **B, C** *Ccl4* and *Ccl5* RNA expression in the optic nerves of *Nf1*-OPG mice treated with IgG, α -TIGIT, α -PD1 or a combination of α -PD1 and α -TIGIT antibodies. Data are represented relative to the IgG control group (IgG, *n* = 5, 2 pooled optic nerves per sample; α -TIGIT *n* = 5, 2 pooled optic nerves per sample; α -PD1, *n* = 4, 2 pooled optic nerves per sample; α -PD1 + TIGIT, *n* = 4, 2 pooled optic nerves per sample). Data are represented as mean \pm SD. A one-way ANOVA test was performed followed by a Dunnett's post test correction. Exact *P* values are indicated. **D** Immunocytochemistry and quantification of proliferating (%Ki67⁺) optic glioma tumor cells (o-GTCs) treated with TCM from unstimulated (none) and exhausted (α -CD3+ α -CD28 antibody stimulated) CD8⁺ T cells (Control, *n* = 8; TCM none, *n* = 4; TCM α -CD3+ α -CD28, *n* = 4). Data are represented as mean \pm SD. A one-way ANOVA test was performed followed by a Dunnett's post-test correction. Exact *P* values are indicated. Scale bar, 200 μ m. **E** Volcano plot showing fold change and *P* value comparing CD8⁺ PD1⁺ T cells (corresponds to the dataset shown in Fig. 2; *n* = 10 pooled mice) and in CD8⁺ PD1⁺ T cells (corresponds to the dataset shown in Fig. 2; *n* = 10 pooled mice) the optic nerve of 12-week-old *Nf1*-OPG mice. Upregulated genes in red, downregulated genes in blue. Differential analyses were performed using gene specific analysis (GSA). **F** Graph showing levels of secreted TGF β in the TCM of unstimulated (none) and exhausted (α -CD3+ α -CD28

antibody stimulated) CD8⁺ T cells by ELISA (none, *n* = 4; α -CD3+ α -CD28, *n* = 4). Data are represented as mean \pm SD. To evaluate statistical differences, a two-tailed non-parametric Mann–Whitney test was performed. Exact *P* values are indicated.

G *Tgfb1* RNA expression in the optic nerves of *Nf1*-OPG mice treated with IgG, α -TIGIT, α -PD1 or a combination of α -PD1 and α -TIGIT antibodies. Data are represented relative to the IgG control group (IgG, *n* = 5, 2 pooled optic nerves per sample; α -TIGIT *n* = 5, 2 pooled optic nerves per sample; α -PD1, *n* = 4, 2 pooled optic nerves per sample; α -PD1 + TIGIT, *n* = 4, 2 pooled optic nerves per sample). Data are represented as mean \pm SD. A one-way ANOVA test was performed followed by a Holm–Šidák post-test correction. Exact *P* values are indicated. **H** Schematic representation of the anti-TGF β treatment (α -TGF β). *Nf1*-OPG mice were treated (200 μ g/dose, i.p., twice per week) from 12 to 16 weeks of age, tissues were analyzed at 16 weeks. The control group was injected with anti-IgG isotype control antibodies. Created in BioRender. Chatterjee, J. (2024) BioRender.com/z17k582.

I Immunohistochemistry and quantification of proliferating (%Ki67⁺) cells in the optic nerves of *Nf1*-OPG mice (IgG, *n* = 5 mice; α -TGF β , *n* = 4 mice). Data are represented as mean \pm SD. To evaluate statistical differences, a two-tailed non-parametric Mann–Whitney test was performed. Exact *P* values are indicated. Scale bar, 200 μ m. **J** Immunohistochemistry and quantification of CD8⁺ T cells in the entire optic nerve of *Nf1*-OPG mice (IgG, *n* = 5 mice; α -TGF β , *n* = 4 mice). Data are represented as mean \pm SD. To evaluate statistical differences, a two-tailed non-parametric Mann–Whitney test was performed. Exact *P* values are indicated. Scale bar, 200 μ m. **K** Schematic representation of the direct and indirect mechanisms by which CD8⁺ exhausted T cells regulate *Nf1*-OPG growth. Created in BioRender. Chatterjee, J. (2024) BioRender.com/z17k582.

immunostained with the primary antibodies listed in Supplementary Table 1. Development was performed using the Vectastain ABC kit (Vector Laboratories, PK4000) and appropriate biotinylated secondary antibodies (Vector Laboratories) or Alexa-fluor-conjugated secondary antibodies (Supplementary Table 1)²². Slides were imaged with a Leica ICC50W microscope using LAS EZ software, or with a Leica DFC3000G fluorescent microscope using LAS X software, or with a Thunder Imager 3D assay using LAS AF Lite 3.2.0 software. Skullcaps were harvested, and meningeal duras were peeled and stained as previously described⁶⁸. Four sites in the superior sagittal sinus were imaged using a Zeiss LSM 880 confocal microscope (Washington University Center for Cellular Imaging).

RNA extraction and real-time RT-qPCR

RNA was isolated from optic nerves using the NucleoSpin RNA Plus kit (Takara-740984.205) according to the manufacturer's instructions. For each experiment, two mice were used per sample. Total RNA was reverse transcribed into cDNA using the High-Capacity cDNA Reverse Transcription Kit (Applied Biosystems, 4368814). Real-time quantitative PCR (RT-qPCR) was performed by TaqMan gene expression (*Alox1*, *Bap1*, *Ccl4*, *Ccl5*, *Ccl2*, *Ccl12*, *Cxcl9*, *Cxcl13*, *Cd274*, *Gapdh*, *Gpx4*, *Gzmb*, *Gzmk*, *Ifng*, *Nectin2*, *Pdcdlg2*, *Prfl*, *Pvr*, *Slc7a11*; Supplementary Table 2) using the TaqMan Fast Advanced Master Mix (Applied Biosystems). All reactions were performed using the QuantStudio 3 (Applied Biosystems) system. $\Delta\Delta$ CT values were calculated using *Gapdh* as an internal control.

Flow cytometry

Dissociated frozen tumor single cells from de-identified human PA samples (clinical information in Supplemental Table 3) were acquired under an approved Human Studies Protocol as from the St. Louis Children's Hospital Pediatric Tumor Bank. The frozen dissociated tumor single cells were thawed and resuspended in DMEM with 10% FBS. Blood, deep cervical lymph nodes, meninges, and optic nerve single cell isolations were generated from 12-week-old WT, *Nf1*^{+/−}, *Nf1*-OPG, *Nf1*^{816C} mice and *Nf1*^{1809C} mice were performed as previously described⁶⁸. Red blood cells (RBC) were lysed with ACK lysis buffer (Quality Biological) and aspirated from the cell pellet. Once single cell suspensions were obtained, they were resuspended in fluorescence activated cell sorting (FACS) buffer on ice and incubated with the Zombie NIR Fixable Viability Kit (BioLegend, 423105). Samples were

resuspended in FACS buffer with CD16/32 (FC block; BioLegend, 101302) or Human TruStain FcX (Fc Receptor Blocking Solution; BioLegend, 422301) for 15 min and fluorescently conjugated antibodies (Supplementary Table 1) on ice were added for 20 min. Samples were washed in FACS buffer, run on a Cytex Aurora spectral flow cytometer (Cytex) (Siteman Flow Cytometry Core), and analyzed using FlowJo software (Tree Star) (Supplementary Fig. 12).

scRNA sequencing and analysis

Dissociated cells from de-identified human PA samples (four female sporadic PAs and one female NF1-PA; clinical information in Supplemental Table 3) previously banked in the St. Louis Children's Hospital Tumor Repository and obtained following appropriate patient consent under an approved Human Studies Protocol, were used for these experiments. The frozen dissociated tumor single cells were thawed and resuspended in DMEM. The cells were then stained with 7-Aminoactinomycin D (7-AAD) (Fisher Scientific, A1310) for sorting using the MoFlo (Siteman Flow Cytometry Core at the Washington University in St. Louis). Live cells were collected and submitted for single cell RNA sequencing (scRNAseq).

Nf1-OPG optic nerves and meningeal dura specimens were collected separately from ten 12-week-old mice and pooled to prepare a single-cell suspension. Optic nerves were collected and dissociated using the neural dissociation kit (Miltenyi Biotec, 130-095-942) followed by debris (Miltenyi Biotec, 130-107-677) and myelin (Miltenyi Biotec, 130-096-733) removal. Single cell suspensions from meningeal dural tissue were prepared as described above, stained with 7-AAD, and sorted using MoFlo. Live cells were collected and sent for scRNA sequencing with TCR V(D)J enrichment.

Single-cell data processing, filtering, cohort data integration, and dimension reduction

For all samples, raw sequencing data was processed using the 10X Genomics Cell Ranger pipeline (version 6.1.1) to generate gene count matrices, and then aligned to the mm10-2020-A (mouse) or GRCh38 (human). All single cell RNA sequencing data were analyzed using Partek Flow software (version 10.0.23). Cell quality was evaluated by the number of reads, detected gene counts, and percentages of mitochondrial reads, followed by CPM (counts per million) normalization. To account for library chemistry and other possible unknown

differences between experiments, cells were integrated using the Seurat3 integration method to produce batch-corrected data. PCA analysis followed by graph-based clustering using Louvain algorithm and t-SNE/UMAP generation employing Euclidean distance were conducted on the first 20 principal components of the integrated expression data. To filter T cells from the datasets, clusters containing increased expression of CD3 genes were selected. Differential analyses were performed using gene specific analysis (GSA), and the results were filtered for genes with P values < 0.05 , and fold changes either less than or equal to -2 or greater than or equal to 2 . Pathway analyses were performed using DAVID Bioinformatics platform, and the significant pathways were selected by $FDR < 0.1$. Gene expression and TCR V(D)J data were overlaid by R scRepertoire package.

T cell isolation

$Nf1^{+/+}$ mouse spleens were homogenized into single cell suspensions by digestion in MACS buffer (Miltenyi Biotec, 130-091-222) with 3% BSA (Miltenyi Biotec, 130-091-376). Erythrocytes were lysed using RBC lysis buffer (eBioscience, 00433357). $CD8^+$ T cells were isolated by selection using a $CD8a$ T cell isolation kit (Miltenyi Biotec, 130-104-075). T cells were maintained at 2.5×10^6 cells/ml in RPMI-1640 medium supplemented with 10% FBS and 1% P/S. To mimic T cell exhaustion in vitro, $CD8^+$ T cells were chronically stimulated every other day with α -mouse CD3 (Fisher Scientific, 16-0031-85) and α -mouse CD28 (Fisher Scientific, 16-0281-82)⁶⁹. The NFAT1 inhibitor FK-506 (F4679) was purchased from Sigma-Aldrich.

ELISA

T cell conditioned media (TCM) from non-stimulated, exhausted (α -CD3+ α -CD28 antibody stimulated), and exhausted (α -CD3+ α -CD28 antibody stimulated) + FK-506 (10 μ M) T cells were collected. Ccl4 and TGF β in the TCM were detected using the mouse CCL4/MIP-1 beta Quantikine ELISA Kit (R&D Systems, MMB00) or the Mouse TGF β ELISA Kit (Abcam, ab119557) according to the manufacturer's instructions. Data from all of these colorimetric assays were collected on an Infinite M Nano (Tecan) microplate reader and analyzed using Magellan Pro 7.4 (Tecan) software.

Migration assays

5×10^5 T cells were added to the upper chamber of a transwell chamber (Corning, 6.5 mm insert, 3.0 μ m polycarbonate membrane, CLS3398-2EA) with 200 μ l serum free PRIM 1640 media. 500 μ l of chemoattractant media (Ccl12 [25 ng/ml, 428-P5-025- R&D systems³²] and Cxcl13 [1 μ g/ml, 470-BC-025- R&D systems]⁷⁰) was added to the lower chamber, and the number of T cells in the lower chambers counted 6 h later.

Optic glioma tumor cell (o-GTC) proliferation and apoptosis assays

10^4 o-GTCs were plated into 12-well plates coated with fibronectin (10 μ g/ml) in complete NSC medium. O-GTCs were incubated with complete NSC medium, TCM from non-stimulated $CD8^+$ T cells, and TCM from exhausted (α -CD3+ α -CD28 antibody stimulated) $CD8^+$ T cells for 48 h. Cells were fixed in 4% paraformaldehyde (PFA), and proliferation and apoptosis quantitated using the primary antibodies listed in Supplementary Table 1. Cells were labeled with secondary Alexa-fluor-conjugated secondary antibodies (Supplementary Table 1). The cells were imaged with a Leica DFC3000G fluorescent microscope using LAS X software.

Statistical analysis

Data were analyzed using GraphPad Prism software (GraphPad Prism 9.3.1). To determine differences between two groups, a two-tailed Mann–Whitney test was used, whereas multiple comparisons were analyzed using a one-way analysis of variance (ANOVA) with Dunnett's,

Tukey's, Holm–Šidák multiple comparisons test. Statistical significance was set at $P \leq 0.05$. All experiments were independently repeated at least three times. Numbers (n) are noted for each individual analysis.

Reporting summary

Further information on research design is available in the Nature Portfolio Reporting Summary linked to this article.

Data availability

The single cell RNA sequencing datasets generated in this study have been deposited in GEO database under accession code [GSE244433](https://doi.org/10.1038/s41467-024-54569-4). Publicly available datasets that passed quality control included two different PA datasets (GSE222850 and dbGAP phs001854.v1.p1) and three different glioblastoma datasets (GSE102130, Annotare [ArrayExpress] accession # E-MTAB-9435, and GSE138794). All other data are available in the article and its Supplementary files or from the corresponding author upon request. Source data are provided with this paper.

References

- Weller, M. et al. Glioma. *Nat. Rev. Dis. Prim.* **10**, 33 (2024).
- Claus, E. B. et al. Survival and low-grade glioma: the emergence of genetic information. *Neurosurg. Focus* **38**, E6 (2015).
- Cordell, E. C., Alghamri, M. S., Castro, M. G. & Gutmann, D. H. T lymphocytes as dynamic regulators of glioma pathobiology. *Neuro Oncol.* **24**, 1647–1657 (2022).
- Robinson, M. H. et al. Subtype and grade-dependent spatial heterogeneity of T-cell infiltration in pediatric glioma. *J. Immunother. Cancer* **8**, e001066 (2020).
- Chen, J. et al. Immune cell analysis of pilocytic astrocytomas reveals sexually dimorphic brain region-specific differences in T-cell content. *Neurooncol. Adv.* **3**, vdab068 (2021).
- Peng, F. et al. Regulated cell death (RCD) in cancer: key pathways and targeted therapies. *Signal Transduct. Target Ther.* **7**, 286 (2022).
- Zhang, W. et al. Pan-cancer evaluation of regulated cell death to predict overall survival and immune checkpoint inhibitor response. *NPJ Precis Oncol.* **8**, 77 (2024).
- Cloughesy, T. F. et al. Neoadjuvant anti-PD-1 immunotherapy promotes a survival benefit with intratumoral and systemic immune responses in recurrent glioblastoma. *Nat. Med.* **25**, 477–486 (2019).
- Reardon, D. A. et al. Effect of nivolumab vs bevacizumab in patients with recurrent glioblastoma: The checkmate 143 phase 3 randomized clinical trial. *JAMA Oncol.* **6**, 1003–1010 (2020).
- Wang, E. J. et al. Immunotherapy resistance in glioblastoma. *Front Genet* **12**, 750675 (2021).
- Naulaerts, S. et al. Multiomics and spatial mapping characterizes human $CD8^+$ T cell states in cancer. *Sci. Transl. Med.* **15**, eadd1016 (2023).
- Sigaud, R. et al. MAPK inhibitor sensitivity scores predict sensitivity driven by the immune infiltration in pediatric low-grade gliomas. *Nat. Commun.* **14**, 4533 (2023).
- Reitman, Z. J. et al. Mitogenic and progenitor gene programmes in single pilocytic astrocytoma cells. *Nat. Commun.* **10**, 3731 (2019).
- Wang, L. et al. The phenotypes of proliferating glioblastoma cells reside on a single axis of variation. *Cancer Discov.* **9**, 1708–1719 (2019).
- Mahlokozera, T. et al. Competitive binding of E3 ligases TRIM26 and WWP2 controls SOX2 in glioblastoma. *Nat. Commun.* **12**, 6321 (2021).
- Filbin, M. G. et al. Developmental and oncogenic programs in H3K27M gliomas dissected by single-cell RNA-seq. *Science* **360**, 331–335 (2018).
- Bajenaru, M. L. et al. Optic nerve glioma in mice requires astrocyte Nf1 gene inactivation and Nf1 brain heterozygosity. *Cancer Res.* **63**, 8573–8577 (2003).

18. Listernick, R., Louis, D. N., Packer, R. J. & Gutmann, D. H. Optic pathway gliomas in children with neurofibromatosis 1: Consensus statement from the NF1 Optic Pathway Glioma Task Force. *Ann. Neurol.* **41**, 143–149 (1997).
19. Hegedus, B. et al. Preclinical cancer therapy in a mouse model of neurofibromatosis-1 optic glioma. *Cancer Res.* **68**, 1520–1528 (2008).
20. Guo, X., Pan, Y. & Gutmann, D. H. Genetic and genomic alterations differentially dictate low-grade glioma growth through cancer stem cell-specific chemokine recruitment of T cells and microglia. *Neuro Oncol.* **21**, 1250–1262 (2019).
21. Anastasaki, C. et al. Neuronal hyperexcitability drives central and peripheral nervous system tumor progression in models of neurofibromatosis-1. *Nat. Commun.* **13**, 2785 (2022).
22. Guo, X. et al. Midkine activation of CD8(+) T cells establishes a neuron-immune-cancer axis responsible for low-grade glioma growth. *Nat. Commun.* **11**, 2177 (2020).
23. Carlino, M. S., Larkin, J. & Long, G. V. Immune checkpoint inhibitors in melanoma. *Lancet* **398**, 1002–1014 (2021).
24. Provencio, M. et al. Perioperative nivolumab and chemotherapy in stage III non-small-cell lung cancer. *N. Engl. J. Med.* **389**, 504–513 (2023).
25. Wherry, E. J. T cell exhaustion. *Nat. Immunol.* **12**, 492–499 (2011).
26. Zheng, L. et al. Pan-cancer single-cell landscape of tumor-infiltrating T cells. *Science* **374**, abe6474 (2021).
27. Gupta, P. K. et al. CD39 expression identifies terminally exhausted CD8+ T cells. *PLoS Pathog.* **11**, e1005177 (2015).
28. Miller, B. C. et al. Subsets of exhausted CD8(+) T cells differentially mediate tumor control and respond to checkpoint blockade. *Nat. Immunol.* **20**, 326–336 (2019).
29. Solga, A. C. et al. RNA sequencing of tumor-associated microglia reveals Ccl5 as a stromal chemokine critical for neurofibromatosis-1 glioma growth. *Neoplasia* **17**, 776–788 (2015).
30. Toonen, J. A. et al. NF1 germline mutation differentially dictates optic glioma formation and growth in neurofibromatosis-1. *Hum. Mol. Genet.* **25**, 1703–1713 (2016).
31. Li, K. et al. Mice with missense and nonsense NF1 mutations display divergent phenotypes compared with human neurofibromatosis type I. *Dis. Model Mech.* **9**, 759–767 (2016).
32. de Andrade Costa, A. et al. Immune deconvolution and temporal mapping identifies stromal targets and developmental intervals for abrogating murine low-grade optic glioma formation. *Neurooncol Adv.* **4**, vdb194 (2022).
33. Chen, Y. H. et al. Mouse low-grade gliomas contain cancer stem cells with unique molecular and functional properties. *Cell Rep.* **10**, 1899–1912 (2015).
34. Anastasaki, C. et al. NF1 mutation-driven neuronal hyperexcitability sets a threshold for tumorigenesis and therapeutic targeting of murine optic glioma. *Neuro Oncol.* **26**, 1496–1508 (2024).
35. Chatterjee, J. et al. Asthma reduces glioma formation by T cell decorin-mediated inhibition of microglia. *Nat. Commun.* **12**, 7122 (2021).
36. Toonen, J. A., Ma, Y. & Gutmann, D. H. Defining the temporal course of murine neurofibromatosis-1 optic gliomagenesis reveals a therapeutic window to attenuate retinal dysfunction. *Neuro Oncol.* **19**, 808–819 (2017).
37. de Blank, P. M. K. et al. Optic pathway gliomas in neurofibromatosis type 1: An update: surveillance, treatment indications, and biomarkers of vision. *J. Neuroophthalmol.* **37**, S23–S32 (2017).
38. Salman, S. et al. HIF inhibitor 32-134D eradicates murine hepatocellular carcinoma in combination with anti-PD1 therapy. *J. Clin. Invest.* **132**, e156774 (2022).
39. Wang, Z. et al. Paradoxical effects of obesity on T cell function during tumor progression and PD-1 checkpoint blockade. *Nat. Med.* **25**, 141–151 (2019).
40. van der Leun, A. M., Thommen, D. S. & Schumacher, T. N. CD8(+) T cell states in human cancer: insights from single-cell analysis. *Nat. Rev. Cancer* **20**, 218–232 (2020).
41. Li, Z., Liu, X., Guo, R. & Wang, P. TIM-3 plays a more important role than PD-1 in the functional impairments of cytotoxic T cells of malignant Schwannomas. *Tumour Biol.* **39**, 1010428317698352 (2017).
42. Adorno Febles, V. R. et al. Single-cell analysis of localized prostate cancer patients links high Gleason score with an immunosuppressive profile. *Prostate* **83**, 840–849 (2023).
43. Milde, T. et al. Reimagining pilocytic astrocytomas in the context of pediatric low-grade gliomas. *Neuro Oncol.* **23**, 1634–1646 (2021).
44. Tang, Y. & Gutmann, D. H. Neurofibromatosis type 1-associated optic pathway gliomas: Current challenges and future prospects. *Cancer Manag. Res.* **15**, 667–681 (2023).
45. Wherry, E. J. & Kurachi, M. Molecular and cellular insights into T cell exhaustion. *Nat. Rev. Immunol.* **15**, 486–499 (2015).
46. Lee, J. et al. Sex-biased T-cell exhaustion drives differential immune responses in glioblastoma. *Cancer Discov.* **13**, 2090–2105 (2023).
47. Kumagai, S. et al. The PD-1 expression balance between effector and regulatory T cells predicts the clinical efficacy of PD-1 blockade therapies. *Nat. Immunol.* **21**, 1346–1358 (2020).
48. Hanggi, K. & Ruffell, B. Cell death, therapeutics, and the immune response in cancer. *Trends Cancer* **9**, 381–396 (2023).
49. Alspach, E. et al. MHC-II neoantigens shape tumour immunity and response to immunotherapy. *Nature* **574**, 696–701 (2019).
50. Chan, I. S. et al. Cancer cells educate natural killer cells to a metastasis-promoting cell state. *J. Cell Biol.* **219**, e202001134 (2020).
51. Hambardzumyan, D., Gutmann, D. H. & Kettenmann, H. The role of microglia and macrophages in glioma maintenance and progression. *Nat. Neurosci.* **19**, 20–27 (2016).
52. Massague, J. TGFbeta in cancer. *Cell* **134**, 215–230 (2008).
53. Liu, S., Ren, J. & Ten Dijke, P. Targeting TGFbeta signal transduction for cancer therapy. *Signal Transduct. Target Ther.* **6**, 8 (2021).
54. Metropulos, A. E., Munshi, H. G. & Principe, D. R. The difficulty in translating the preclinical success of combined TGFbeta and immune checkpoint inhibition to clinical trial. *EBioMedicine* **86**, 104380 (2022).
55. Wick, A. et al. Phase 1b/2a study of galunisertib, a small molecule inhibitor of transforming growth factor-beta receptor I, in combination with standard temozolomide-based radiochemotherapy in patients with newly diagnosed malignant glioma. *Invest. N. Drugs* **38**, 1570–1579 (2020).
56. Malek, E. et al. The TGFbeta type I receptor kinase inhibitor vactosertib in combination with pomalidomide in relapsed/refractory multiple myeloma: a phase 1b trial. *Nat. Commun.* **15**, 7388 (2024).
57. Kim, B. G., Malek, E., Choi, S. H., Ignatz-Hoover, J. J. & Driscoll, J. J. Novel therapies emerging in oncology to target the TGF-beta pathway. *J. Hematol. Oncol.* **14**, 55 (2021).
58. Gu-Trantien, C. et al. CD4(+) follicular helper T cell infiltration predicts breast cancer survival. *J. Clin. Invest.* **123**, 2873–2892 (2013).
59. Bindea, G. et al. Spatiotemporal dynamics of intratumoral immune cells reveal the immune landscape in human cancer. *Immunity* **39**, 782–795 (2013).
60. Aoki, T. et al. Spatially resolved tumor microenvironment predicts treatment outcomes in relapsed/refractory Hodgkin lymphoma. *J. Clin. Oncol.* **42**, 1077–1087 (2024).
61. Gunn, M. D. et al. A B-cell-homing chemokine made in lymphoid follicles activates Burkitt's lymphoma receptor-1. *Nature* **391**, 799–803 (1998).
62. Goswami, S. et al. ARID1A mutation plus CXCL13 expression act as combinatorial biomarkers to predict responses to immune checkpoint therapy in mUCC. *Sci. Transl. Med.* **12**, eabc4220 (2020).

63. Belcaid, Z. et al. Low-dose oncolytic adenovirus therapy overcomes tumor-induced immune suppression and sensitizes intracranial gliomas to anti-PD-1 therapy. *Neurooncol Adv.* **2**, vdaa011 (2020).
64. Dixon, K. O. et al. Functional anti-TIGIT antibodies regulate development of autoimmunity and antitumor immunity. *J. Immunol.* **200**, 3000–3007 (2018).
65. Ariyan, C. E. et al. Robust antitumor responses result from local chemotherapy and CTLA-4 blockade. *Cancer Immunol. Res.* **6**, 189–200 (2018).
66. O'Sullivan, T. et al. Cancer immunoediting by the innate immune system in the absence of adaptive immunity. *J. Exp. Med.* **209**, 1869–1882 (2012).
67. Manlove, L. S. et al. Adaptive immunity to leukemia is inhibited by cross-reactive induced regulatory T cells. *J. Immunol.* **195**, 4028–4037 (2015).
68. Rustenhoven, J. et al. Functional characterization of the dural sinuses as a neuroimmune interface. *Cell* **184**, 1000–1016 e1027 (2021).
69. Vardhana, S. A. et al. Impaired mitochondrial oxidative phosphorylation limits the self-renewal of T cells exposed to persistent antigen. *Nat. Immunol.* **21**, 1022–1033 (2020).
70. Klasen, C. et al. MIF promotes B cell chemotaxis through the receptors CXCR4 and CD74 and ZAP-70 signaling. *J. Immunol.* **192**, 5273–5284 (2014).

Acknowledgements

We thank all members of the Gutmann laboratory and Dr. Robert Schreiber for their helpful suggestions and scientific discussions. We thank Dr. David Limbrick and Corrine Gardner for providing the human PA samples. This work was funded by a grant from the National Cancer Institute (CA261939 to D.H.G.). We thank the Alvin J. Siteman Cancer Center at Washington University School of Medicine and Barnes-Jewish Hospital in St. Louis, MO., for the use of the Siteman Flow Cytometry (NCI Cancer Center Support Grant P30 CA091842). Imaging using the Zeiss LSM 880 Airyscan Confocal Microscope was performed in part through the use of Washington University Center for Cellular Imaging (WUCCI) supported by Washington University School of Medicine. We thank The Children's Discovery Institute of Washington University and St. Louis Children's Hospital (CDI-CORE-2015-505 and CDI-CORE-2019-813) and the Foundation for Barnes-Jewish Hospital (3770 and 4642). Confocal super-resolution data was generated on a Zeiss LSM 880 Airyscan Confocal Microscope, purchased with support from the Office of Research Infrastructure Programs (ORIP), a part of the NIH Office of the Director (OD021629). We thank the Genome Technology Access Center at the McDonnell Genome Institute at Washington University School of Medicine for help with genomic analysis. The Center is partially supported by NCI Cancer Center Support Grant #P30 CA91842 to the Siteman Cancer Center from the National Center for Research Resources (NCRR), a component of the National Institutes of Health (NIH), and NIH Roadmap for Medical Research. This publication is solely the responsibility of the authors and does not necessarily represent the official view of NCRR or NIH. The Washington University Ophthalmology

Core facility is funded by the National Eye Institute (P30EY002687). Figures 3A, 4A, 5B, 5D, 6A, G, 7H, K, Supplementary Fig. 7A, and Supplementary Fig. 11A were created with BioRender.com. We thank Andrew Hunt and Rujuta Idade with their assistance in the RT-qPCR and IHC experiments.

Author contributions

R.B. and D.H.G. designed and analyzed the experiments. R.B., J.C., X.Q., X.G., I.S., K.G., A.B., J.K. conducted and/or interpreted the experiments. R.M., and O.C. performed the scRNAseq analyses. The manuscript was assembled by R.B. and D.H.G. D.H.G. was responsible for the final production of the manuscript. All authors have read and approved the final manuscript.

Competing interests

The authors declare no competing interests.

Additional information

Supplementary information The online version contains supplementary material available at <https://doi.org/10.1038/s41467-024-54569-4>.

Correspondence and requests for materials should be addressed to David H. Gutmann.

Peer review information *Nature Communications* thanks the anonymous reviewer(s) for their contribution to the peer review of this work. A peer review file is available.

Reprints and permissions information is available at <http://www.nature.com/reprints>

Publisher's note Springer Nature remains neutral with regard to jurisdictional claims in published maps and institutional affiliations.

Open Access This article is licensed under a Creative Commons Attribution-NonCommercial-NoDerivatives 4.0 International License, which permits any non-commercial use, sharing, distribution and reproduction in any medium or format, as long as you give appropriate credit to the original author(s) and the source, provide a link to the Creative Commons licence, and indicate if you modified the licensed material. You do not have permission under this licence to share adapted material derived from this article or parts of it. The images or other third party material in this article are included in the article's Creative Commons licence, unless indicated otherwise in a credit line to the material. If material is not included in the article's Creative Commons licence and your intended use is not permitted by statutory regulation or exceeds the permitted use, you will need to obtain permission directly from the copyright holder. To view a copy of this licence, visit <http://creativecommons.org/licenses/by-nc-nd/4.0/>.

© The Author(s) 2024